Imperfection sensitivity of thin-walled rectangular hollow section struts susceptible to interactive buckling

Jiajia Shen, M. Ahmer Wadee*

Department of Civil and Environmental Engineering, Imperial College London, South Kensington Campus, London SW7 2AZ, UK

Abstract

A variational model describing the interactive buckling of thin-walled rectangular hollow section struts with geometric imperfections is developed based on analytical techniques. A system of nonlinear differential and integral equilibrium equations is derived and solved using numerical continuation. Imperfection sensitivity studies focus on the cases where the global and local buckling loads are close. The equilibrium behaviour of struts with varying imperfection sizes, characterized by the equilibrium paths and the progressive change in local buckling wavelength, is highlighted and compared. The numerical results reveal that struts exhibiting mode interaction are very sensitive to both local and global imperfections. The results from the variational model are verified using the finite element method in conjunction with the static Riks method and show good comparisons. A simplified method to calculate the pitchfork bifurcation load where mode interaction is triggered for struts with a global imperfection is developed for the first time. The simplified method is calibrated to predict the ultimate load for struts with tolerance level global imperfections and combined imperfections based on the parametric study, which also reveals that local and global imperfections are relatively more significant where global and local buckling are critical respectively. Finally, the ultimate load for struts with tolerance level geometric imperfections is compared with the existing Direct Strength Method (DSM). Potential dangers of making unsafe load-carrying capacity predictions by the DSM are highlighted and an improved strength equation is proposed.

Keywords: Mode interaction; Geometric imperfections; Length effects; Direct Strength Method.

1. Introduction

Buckling instabilities are the principal failure mode for structural members made from high-strength lightweight materials [1, 2, 3, 4]. Moreover, compression members made

*Corresponding author

Email addresses: j.shen14@imperial.ac.uk (Jiajia Shen), a.wadee@imperial.ac.uk (M. Ahmer Wadee)

from thin-walled plated elements are vulnerable to a variety of different elastic instability phenomena [5, 6, 7, 8, 9, 10]. In practice, since the post-buckling behaviour of plates is stable, the post-buckling strength of such elements is included in design codes for this to be exploited and hence make more efficient use of the material [11, 12]. Even though the possible individual buckling modes taken in isolation are stable or neutral in terms of their post-buckling behaviour, the triggering of various combinations of modes simultaneously can lead to a violent destabilization after the ultimate load is reached [13, 14, 15, 16, 17]. More importantly, such structural components tend to be highly sensitive to imperfections [18, 19, 20, 21, 22, 23, 24, 25]; a tiny imperfection may lead to a significant erosion in the load-carrying capacity.

Early work investigating the imperfection sensitivity of thin-walled plated structures exhibiting mode interaction was conducted by van der Neut [5]. Using a simplified model comprising two load-carrying flanges and a pair of rigid webs with no longitudinal stiffness, the erosion of load-carrying capacity due to local and global geometric imperfections was investigated. It was found that when the ratio of the global buckling load to the local buckling load is close to unity, the aforementioned erosion is significant and the failure may be explosive due to a snap-back instability. It was also identified that the erosion is principally derived from local imperfections in the flanges. However, owing to the increased technical complexity, the local imperfections in the flange were limited to the eigenmode corresponding to the lowest local buckling load. Using largely the same methodology, Koiter and Pignataro [18] also identified the sensitivity of stiffened plates to both local and global imperfections. However, their findings emphasized that the effects identified in [5] were perhaps overestimated by the classical asymptotic formulae, except for vanishingly small imperfections.

Wadee and his collaborators have developed a series of analytical models to study the imperfection sensitivity of sandwich panels [22], stiffened plates [24] and I-section struts [23, 25] that exhibit mode interaction. It has been determined that these compression members are sensitive to both local and global geometric imperfections. Moreover, using the form of the local imperfection that matches the least stable localized post-buckling mode for the strut on a softening foundation closely – derived from a first order approximation of a multiple scale perturbation analysis [22], the worst form of the local imperfections has been identified in terms of the initial wavelength, amplitude and degree of localization. It has also been found that the localized imperfection may be even more severe than those that are affine to the local buckling eigenmodes, particularly for cases where the imperfection sizes are practically realistic.

Previous work, specifically on imperfection sensitivity in box-section columns, has mainly concerned short columns, where the local buckling stress is very close to the material yield stress. Graves Smith [26] developed an analytical model based on variational principles to investigate the effects of geometric imperfections and residual stresses on the load-carrying capacity of thin-walled welded box-section columns. Material nonlinearity was also considered in the model. Loughlan et al. [27] approached the same problem using the finite element (FE) method. Both works identified characteristic unstable equilibrium paths and confirmed that local imperfections are significant in eroding the load-carrying

capacity.

Maquoi and Massonnet [28] studied the collapse load of square box-section columns with geometric imperfections using the software developed by Klöppel and Schubert [29]. They determined the behaviour in terms of 'efficiency charts' [30], which shows the relationship of the ultimate load for thin-walled struts versus the ratio of the global and local buckling loads under a constant weight constraint for optimum design purposes. They determined that the respective curves were very flat in the vicinity where the local and global buckling loads are equal, signifying that reaching the linear critical buckling load was practically unachievable for such components with realistically sized initial imperfections.

Kiymaz [31] investigated the effects of column out-of-straightness, plate imperfections, residual stresses and material plasticity on the ultimate load and post-buckling behaviour of square hollow section columns exhibiting mode interaction using the finite element (FE) package ABAQUS. Three example columns with typical slendernesses were analysed, where (i) global buckling was clearly critical, (ii) global and local buckling were triggered simultaneously, and (iii) local buckling was clearly critical. The severe erosion in the load-carrying capacity due to imperfections in the case where the local and global buckling loads were the same was again observed.

Degée et al. [32] investigated the effects of various imperfections, *i.e.* residual stresses, local and global geometric imperfections, on the load-carrying capacity of slender welded RHS columns exhibiting mode interaction through experimental and numerical methods. By amplifying the local and global geometric imperfections, they found that a model with a local imperfection of 1/250 of the cross-section width and a global imperfection of 1/725 of the column length showed good agreement with a model including residual stresses.

There has also been a great deal of effort in measuring the local imperfection distribution of thin-walled section members [33, 34, 35]. However, since the geometric imperfections of thin-walled section members are affected by a number of different factors, such as material properties, plate thickness, manufacturing methods and cross-section geometric properties [33], there seems to be no real consensus on a consistent or unified method to determine both the distribution and magnitude of geometric imperfections that reflect imperfections actually found in practice.

The current work extends the previously developed variational models [36, 37] to study the imperfection sensitivity of rectangular hollow section struts exhibiting local–global mode interaction. The developed system of nonlinear ordinary differential and integral equations subject to boundary conditions is solved using the well-known numerical continuation software AUTO-07P [38]. The resulting equilibrium paths are presented for various different cases and the erosion in the load-carrying capacity due to imperfections is observed. The results from the variational model show good comparisons with the numerical results using the FE method in conjunction with the static Riks method [39] developed within the commercial package ABAQUS [40]. A simplified method to calculate the pitchfork bifurcation load where mode interaction is triggered for struts with global imperfections is developed for the first time. The relative significance of global and local imperfections for struts with different lengths is investigated. Based on the numerical results, the simplified method is calibrated to predict the ultimate load for struts with tolerance level global

imperfections and combined local and global imperfections. A parametric study varying the strut length is conducted and a comparison with current design guidelines using the Direct Strength Method (DSM) [41] is made. The potential for making unsafe predictions of actual load-carrying capacity using the current relevant DSM expression is highlighted and a refined equation is proposed for the cases considered. The current work facilitates a better understanding of the imperfection sensitivity of thin-walled rectangular hollow section struts exhibiting mode interaction, which will allow the establishment of more rational and robust design guidance for such structural components in future.

2. Development of the variational model

A thin-walled rectangular hollow section strut of length L with simply-supported boundary conditions under a concentric load P is considered, as shown in Figure 1. The web depth and thickness are d and t_{w} respectively; the flange width and thickness are b and t_{f} respectively. The strut is assumed to be made from a linear elastic, homogeneous and isotropic material with Young's modulus E, Poisson's ratio ν and shear modulus $G = E/\left[2\left(1+\nu\right)\right]$. The joints between the webs and flanges are assumed to be rigid, which implies that the webs and flanges remain perpendicular at their common edges during local buckling [42].

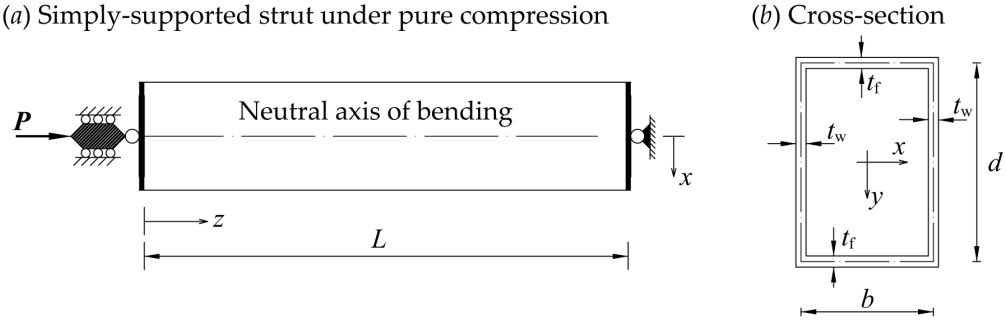

Figure 1: (a) Plan view of the thin-walled rectangular hollow section strut of length L under a concentric load P. The lateral and longitudinal coordinates are x and z respectively. (b) Cross-section geometry of the strut; the vertical coordinate is y.

2.1. Modal descriptions

The description of the global and local modal displacements adopts the same approach as in the recent study for the perfect system [37], as shown in Figure 2. The degrees of freedom known as 'sway' and 'tilt' [43, 13], as shown in Figure 2(a), are introduced in combination to account for the effects of shear, since previous studies [13, 14, 16, 44, 45] have demonstrated that including the induced flexural shear strain in the total potential energy formulation is a way to preserve the terms necessary to model interactive buckling successfully. The pure lateral displacement W and the corresponding pure rotation of the plane section θ are defined by the following expressions:

$$W(z) = -q_s L \sin\left(\frac{\pi z}{L}\right), \quad \theta\left(z\right) = -q_t \pi \cos\left(\frac{\pi z}{L}\right), \tag{1}$$

where q_s and q_t are the generalized coordinates defined as the normalized amplitude of the sway and tilt components of the global buckling mode respectively. The local buckling

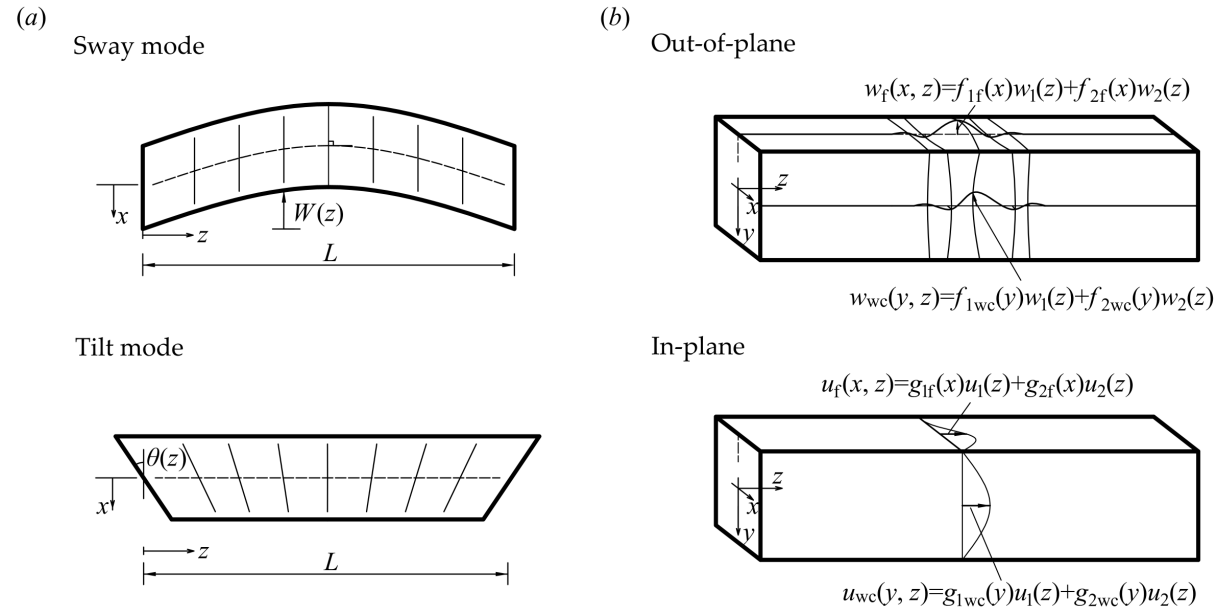

Figure 2: (a) Global buckling mode bending about the weak axis y: sway and tilt components. (b) Local buckling mode: out-of-plane mode in the flanges $w_{\mathrm{f}}(x, z)$ and in the more compressed web $w_{\mathrm{wc}}(y, z)$; in-plane mode in the flanges $u_{\mathrm{f}}(x, z)$ and in the more compressed web $u_{\mathrm{wc}}(y, z)$.

mode, including out-of-plane and in-plane displacements, as shown in Figure 2(b), is expressed as a combination of the modes in the pure local buckling case and the case where global buckling is critical:

$$\begin{aligned}
w_{\mathrm{f}}(x, z) &= f_{1\mathrm{f}}(x)w_1(z) + f_{2\mathrm{f}}(x)w_2(z),\\
w_{\mathrm{wc}}(y, z) &= f_{1\mathrm{wc}}(y)w_1(z) + f_{2\mathrm{wc}}(y)w_2(z),\\
w_{\mathrm{wt}}(y, z) &= f_{1\mathrm{wt}}(y)w_1(z) + f_{2\mathrm{wt}}(y)w_2(z),\\
u_{\mathrm{f}}(x, z) &= g_{1\mathrm{f}}(x)u_1(z) + g_{2\mathrm{f}}(x)u_2(z),\\
u_{\mathrm{wc}}(y, z) &= g_{1\mathrm{wc}}(y)u_1(z) + g_{2\mathrm{wc}}(y)u_2(z),\\
u_{\mathrm{wt}}(y, z) &= g_{1\mathrm{wt}}(y)u_1(z) + g_{2\mathrm{wt}}(y)u_2(z),
\end{aligned} \tag{2}$$

where f and g are the cross-section components for the out-of-plane and in-plane components respectively; w_i and u_i, where $i = \{1, 2\}$, are the longitudinal out-of-plane and in-plane displacement components respectively. Subscripts 1 and 2 represent the cases where the critical buckling modes are local and global respectively, as shown in Figure 3. The subscripts 'f' and 'w' represent the flanges and webs respectively; subscripts 'c' and 't' represent the more and less compressed webs respectively. The cross-section component of the local out-of-plane displacement field, as shown in Figure 3, is estimated by applying

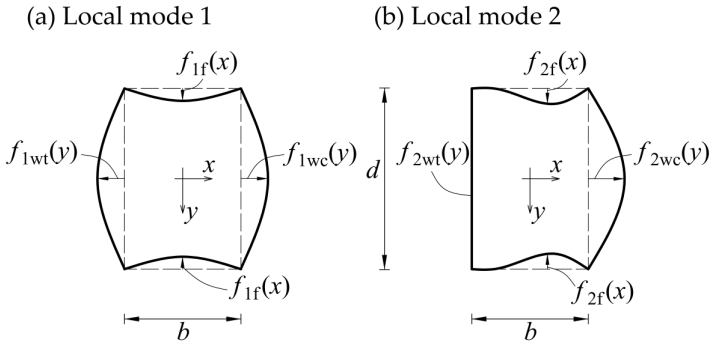

Figure 3: Cross-section components of the local out-of-plane displacement field. (a) Pure local buckling case. (b) Interactive buckling case where global buckling is critical.

appropriate kinematic and static boundary conditions for each plate and their joints in conjunction with the Rayleigh–Ritz method, the detailed derivation of which can be found in previous work [36, 37]:

$$f_{1\mathrm{wc}} = f_{1\mathrm{wt}} = -\frac{4\left(\phi_\mathrm{c}\phi_\mathrm{t}^3+1\right)}{\pi\phi_\mathrm{c}\phi_\mathrm{t}^3-\phi_\mathrm{c}\phi_\mathrm{t}^3-4}\cos\left(\frac{\pi y}{d}\right)+\frac{(3+\pi)\,\phi_\mathrm{c}\phi_\mathrm{t}^3}{\pi\phi_\mathrm{c}\phi_\mathrm{t}^3-\phi_\mathrm{c}\phi_\mathrm{t}^3-4}\left(1-\frac{4y^2}{d^2}\right), \tag{3}$$

$$f_{1\mathrm{f}} = -\frac{4\pi}{\phi_\mathrm{c}\left(\pi\phi_\mathrm{c}\phi_\mathrm{t}^3-\phi_\mathrm{c}\phi_\mathrm{t}^3-4\right)}\left(\frac{x}{b}+\frac{1}{2}\right)\left(\frac{x}{b}-\frac{1}{2}\right), \tag{4}$$

$$f_{2\mathrm{wc}} = \frac{-2\left(2\phi_\mathrm{c}\phi_\mathrm{t}^3+1\right)}{\pi\phi_\mathrm{c}\phi_\mathrm{t}^3-4\phi_\mathrm{c}\phi_\mathrm{t}^3-2}\cos\frac{\pi y}{d}+\frac{\pi\phi_\mathrm{c}\phi_\mathrm{t}^3}{\pi\phi_\mathrm{c}\phi_\mathrm{t}^3-4\phi_\mathrm{c}\phi_\mathrm{t}^3-2}\left(1-\frac{4y^2}{d^2}\right), \tag{5}$$

$$f_{2\mathrm{f}} = -\frac{2\pi}{\phi_\mathrm{c}\left(\pi\phi_\mathrm{c}\phi_\mathrm{t}^3-4\phi_\mathrm{c}\phi_\mathrm{t}^3-2\right)}\left(\frac{x}{b}+\frac{1}{2}\right)^2\left(\frac{x}{b}-\frac{1}{2}\right), \tag{6}$$

$$f_{2\mathrm{wt}} = 0. \tag{7}$$

Here, $\phi_\mathrm{c} = d/b$ is the cross-section aspect ratio and $\phi_\mathrm{t} = t_\mathrm{f}/t_\mathrm{w}$ is the flange–web thickness ratio. It should be mentioned that the above assumption for $f_{1\mathrm{f}}$ and $f_{1\mathrm{w}}$ is only valid for rectangular cross-sections ($d > b$), where the critical local buckling stress for the webs is smaller than that for the flanges. As for the in-plane shape function, a recent numerical study [46] demonstrated that the profile is very close to that of the out-of-plane components. Therefore, these components are in fact assumed to be the same, *i.e.* $g_{i\mathrm{f}} = f_{i\mathrm{f}}$, $g_{i\mathrm{wc}} = f_{i\mathrm{wc}}$ and $g_{i\mathrm{wt}} = f_{i\mathrm{wt}}$. It should be noted that this assumption may not be consistent with classical theory [47], but the shape function forms do satisfy the kinematic boundary conditions. Moreover, since the energy would be minimized by the longitudinal components of the in-plane displacement, *i.e.* $u_1(z)$ and $u_2(z)$, the approximate nature of the shape function should be mitigated somewhat.

2.2. Imperfections description

An initial out-of-straightness in the x-direction, W_0, and an initial pure rotation of the plane section θ_0, corresponding to the sway and tilt global buckling mode in Eq. (1), are introduced to the whole strut respectively as components that form the global imperfection:

$$W_0(z) = -q_{s0} L \sin\left(\frac{\pi z}{L}\right), \quad \theta_0(z) = -q_{t0}\pi \cos\left(\frac{\pi z}{L}\right), \tag{8}$$

with q_{s0} and q_{t0} being the respective normalized amplitudes. A recent study [37] showed that in the transition from the pure local buckling mode, shown in Figure 3(a), to the global buckling induced interactive mode, shown in Figure 3(b), there is a redistribution of stiffness across the cross-section. Specifically, owing to the rigid connection between each individual plates, the less compressed web provides additional restraint to the more compressed side [48, 49, 50, 37]. Hence, there is an effective increase in the axial stiffness of the more compressed web and flanges, thus leading to a higher resistance to compressive stresses. It implies that the mono-symmetric cross-section imperfection profile would be effectively more severe than the doubly-symmetric case. Therefore, the mono-symmetric cross-section deformation profile, as shown in Figure 3(b), is used as the cross-section component for the local imperfection. The local imperfection is introduced by defining an initial out-of-plane deflection in both flanges and webs, corresponding to the local mode description in Eq. (2):

$$w_{\mathrm{f0}}(x,z) = f_{2\mathrm{f}}(x) w_0(z), \quad w_{\mathrm{wc0}}(y,z) = f_{2\mathrm{wc}}(y) w_0(z), \quad w_{\mathrm{wt0}}(y,z) = f_{2\mathrm{wt}}(y) w_0(z), \tag{9}$$

where the cross-section components f are the same as described in Eqs. (5)–(7); the longitudinal component of the local imperfection $w_0(z)$ is derived from a first-order approximation from a multiple scale perturbation analysis of a strut on a nonlinear softening foundation, which has been demonstrated to match the least stable localized post-buckling mode shape very well [51]:

$$w_0(z) = A_0 \operatorname{sech}\left[\alpha\left(\frac{z}{L} - \eta\right)\right] \cos\left[\beta\pi\left(\frac{z}{L} - \eta\right)\right], \tag{10}$$

where $z \in [0, L]$ and the imperfection is symmetric about $z/L = \eta$. Since previous work on sandwich panels [22], I-section struts [23], stiffened plates [24] and functionally graded carbon nanotube-reinforced composite beams [52] have demonstrated that the worst case occurs when the local imperfection is symmetric about midspan, the value of η is selected to be 1/2. The quantity A_0 controls the amplitude of the imperfection component. The parameters α and β control the degree of localization of the imperfection and the number of sinusoidal half waves of the longitudinal imperfection component respectively, as shown in Figure 4. When $\alpha = 0$, the function is periodic; with the increase of α, the function becomes increasingly localized. Moreover, in order to be in accord with the symmetry condition at midspan, β should be an odd number.

2.3. Total potential energy

The total potential energy V of the strut is determined with the principal contributions from the bending energy in both webs due to global buckling, the bending energy in the

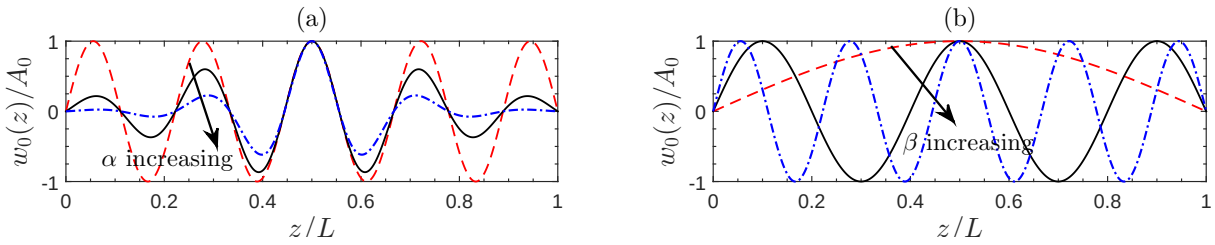

Figure 4: The profile of the normalized local imperfection function, $w_0(z)/A_0$. (a) Localized imperfections introduced by varying the localization parameter α from zero to 10. (b) Periodic imperfections ($\alpha = 0$) with different numbers of half sine waves by varying the frequency parameter β from 1 to 9.

flanges and webs due to local buckling, the membrane strain energy due to both global and local buckling, and the work done by the external load $P\mathcal{E}$, where $\mathcal{E}$ is the total end-shortening. The formulation of the total potential energy functional follows a similar approach, as found in previous work [37], but currently accounts for the scenarios where both global and local geometric imperfections exist. The unloaded strut with initial global and local imperfections is assumed to be stress-relieved [53, 22, 23, 24]. The case of the global imperfection W_0 is illustrated in Figure 5. For the local imperfection case, w_0 would replace W_0 and the flexural rigidity of the flanges $D_\mathrm{f} = Et_\mathrm{f}^3/\left[12\left(1-\nu^2\right)\right]$ or the webs $D_\mathrm{w} = Et_\mathrm{w}^3/\left[12\left(1-\nu^2\right)\right]$ would replace the flexural rigidity of the web about the local weak neutral axis $EI_\mathrm{w} = Edt_\mathrm{w}^3/12$.

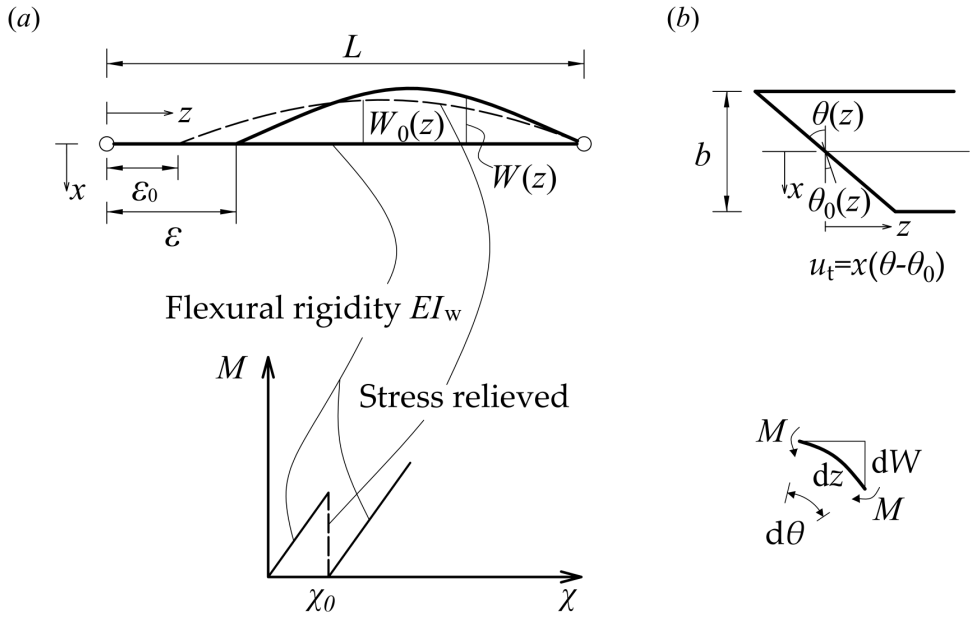

Figure 5: Introduction of the global imperfection. (a) The out-of-straightness sway component W_0 and (b) the pure rotation tilt component θ_0.

It should be stressed that only bending energy stored in the webs contributes to the global bending energy $U_{\mathrm{b,o}}$ through the sway mode, since the membrane energy stored in the flanges accounts for the effect of global bending through the tilt mode, see Figure 2(a). Moreover, since the webs are relatively thin, the shear strain through the thickness may be neglected. Therefore, the global bending energy, $U_{\mathrm{b,o}}$, can be expressed thus:

$$U_{\mathrm{b,o}} = 2\int_0^L \frac{EI_{\mathrm{w}}}{2}\left(\chi - \chi_0\right)^2 \mathrm{d}z = EI_{\mathrm{w}}\int_0^L \left(q_s - q_{s0}\right)^2 \frac{\pi^4}{L^2}\sin^2\frac{\pi z}{L}\,\mathrm{d}z, \tag{11}$$

with $\chi = \ddot{W}$ and $\chi_0 = \ddot{W}_0$, where dots represent derivatives with respect to z. The factor of 2 is included to account for both webs.

The local bending energy stored in both flanges, the more compressed web and the less compressed web can be determined by the standard expression for the strain energy of bending of a plate [54], hence:

$$\begin{aligned} U_{\mathrm{b,fl}} = D_{\mathrm{f}}\int_0^L \int_{-b/2}^{b/2} \Bigg\{ &\left[\frac{\partial^2\left(w_{\mathrm{f}} - w_{\mathrm{f0}}\right)}{\partial z^2} + \frac{\partial^2\left(w_{\mathrm{f}} - w_{\mathrm{f0}}\right)}{\partial x^2}\right]^2 \\ &- 2(1-\nu)\Bigg[\frac{\partial^2\left(w_{\mathrm{f}} - w_{\mathrm{f0}}\right)}{\partial z^2}\frac{\partial^2\left(w_{\mathrm{f}} - w_{\mathrm{f0}}\right)}{\partial x^2} \\ &- \left(\frac{\partial^2\left(w_{\mathrm{f}} - w_{\mathrm{f0}}\right)}{\partial z \partial x}\right)^2\Bigg]\Bigg\}\mathrm{d}x\,\mathrm{d}z, \end{aligned} \tag{12}$$

$$\begin{aligned} U_{\mathrm{b,wcl}} = \frac{D_{\mathrm{w}}}{2}\int_0^L \int_{-d/2}^{d/2} \Bigg\{ &\left[\frac{\partial^2\left(w_{\mathrm{wc}} - w_{\mathrm{wc0}}\right)}{\partial z^2} + \frac{\partial^2\left(w_{\mathrm{wc}} - w_{\mathrm{wc0}}\right)}{\partial y^2}\right]^2 \\ &- 2(1-\nu)\Bigg[\frac{\partial^2\left(w_{\mathrm{wc}} - w_{\mathrm{wc0}}\right)}{\partial z^2}\frac{\partial^2\left(w_{\mathrm{wc}} - w_{\mathrm{wc0}}\right)}{\partial y^2} \\ &- \left(\frac{\partial^2\left(w_{\mathrm{wc}} - w_{\mathrm{wc0}}\right)}{\partial z \partial y}\right)^2\Bigg]\Bigg\}\mathrm{d}y\,\mathrm{d}z, \end{aligned} \tag{13}$$

$$\begin{aligned} U_{\mathrm{b,wtl}} = \frac{D_{\mathrm{w}}}{2}\int_0^L \int_{-d/2}^{d/2} \Bigg\{ &\left[\frac{\partial^2\left(w_{\mathrm{wt}} - w_{\mathrm{wt0}}\right)}{\partial z^2} + \frac{\partial^2\left(w_{\mathrm{wt}} - w_{\mathrm{wt0}}\right)}{\partial y^2}\right]^2 \\ &- 2(1-\nu)\Bigg[\frac{\partial^2\left(w_{\mathrm{wt}} - w_{\mathrm{wt0}}\right)}{\partial z^2}\frac{\partial^2\left(w_{\mathrm{wt}} - w_{\mathrm{wt0}}\right)}{\partial y^2} \\ &- \left(\frac{\partial^2\left(w_{\mathrm{wt}} - w_{\mathrm{wt0}}\right)}{\partial z \partial y}\right)^2\Bigg]\Bigg\}\mathrm{d}y\,\mathrm{d}z. \end{aligned} \tag{14}$$

The membrane strain energy in the flanges $U_{\mathrm{m,f}}$ is derived from considering the direct strains (ε_z) and the shear strains (γ_{xz}) in the flanges. The direct strains comprise three

contributions, the first term from the global tilt mode, the next three terms from the local mode obtained based on von Kármán plate theory and finally a purely in-plane compressive strain Δ:

$$\begin{aligned}\varepsilon_{z,\mathrm{f}} &= \frac{\partial u_t}{\partial z} + \frac{\partial u_\mathrm{f}}{\partial z} + \frac{1}{2}\left(\frac{\partial w_\mathrm{f}}{\partial z}\right)^2 - \frac{1}{2}\left(\frac{\partial w_{\mathrm{f}0}}{\partial z}\right)^2 - \Delta \\ &= -x\left(q_t - q_{t0}\right)\frac{\pi^2}{L}\sin\frac{\pi z}{L} + \left\{g_{1\mathrm{f}}\right\}_x \dot{u}_1 + \left\{g_{2\mathrm{f}}\right\}_x \dot{u}_2 + \frac{1}{2}\left\{f_{1\mathrm{f}}^2\right\}_x \dot{w}_1^2 \\ &\quad + \frac{1}{2}\left\{f_{2\mathrm{f}}^2\right\}_x \left(\dot{w}_2^2 - \dot{w}_0^2\right) + \left\{f_{1\mathrm{f}} f_{2\mathrm{f}}\right\}_x \dot{w}_1 \dot{w}_2 - \Delta. \end{aligned} \tag{15}$$

The shear strain component can be written thus:

$$\begin{aligned}\gamma_{xz,\mathrm{f}} &= \frac{\partial u_\mathrm{f}}{\partial x} + \frac{\partial\left(W - W_0\right)}{\partial z} - \left(\theta - \theta_0\right) + \frac{\partial w_\mathrm{f}}{\partial x}\frac{\partial w_\mathrm{f}}{\partial z} - \frac{\partial w_{\mathrm{f}0}}{\partial x}\frac{\partial w_{\mathrm{f}0}}{\partial z} \\ &= \left\{g_{1\mathrm{f}}'\right\}_x u_1 + \left\{g_{2\mathrm{f}}'\right\}_x u_2 - \left[\left(q_s - q_t\right) - \left(q_{s0} - q_{t0}\right)\right]\pi\cos\frac{\pi z}{L} \\ &\quad + \left\{f_{1\mathrm{f}}' f_{1\mathrm{f}}\right\}_x \dot{w}_1 w_1 + \left\{f_{2\mathrm{f}}' f_{2\mathrm{f}}\right\}_x \left(\dot{w}_2 w_2 - \dot{w}_0 w_0\right) \\ &\quad + \left\{f_{1\mathrm{f}}' f_{2\mathrm{f}}\right\}_x w_1 \dot{w}_2 + \left\{f_{1\mathrm{f}} f_{2\mathrm{f}}'\right\}_x \dot{w}_1 w_2, \end{aligned} \tag{16}$$

where primes denote differentiation with respect to x and the terms in the braces represent a definite integration with respect to the variable denoted by the subscript, thus:

$$\left\{F(x)\right\}_x = \int_{-b/2}^{b/2} F(x)\,\mathrm{d}x, \tag{17}$$

where F is an example function. From the previous numerical study [46], the transverse stress component was shown to be tiny when compared with the longitudinal stress, a finding that also coincides with earlier work [18]. Therefore, the complete expression for the membrane strain energy stored in the flanges can be written thus if the transverse strain is simplified to be $\varepsilon_{x,\mathrm{f}} = -\nu\varepsilon_{z,\mathrm{f}}$:

$$U_{\mathrm{m,f}} = U_{\mathrm{fd}} + U_{\mathrm{fs}} = 2\int_0^L \int_{-t_\mathrm{f}/2}^{t_\mathrm{f}/2} \int_{-b/2}^{b/2} \frac{1}{2}\left(E\varepsilon_{z,\mathrm{f}}^2 + G\gamma_{xz,\mathrm{f}}^2\right)\mathrm{d}x\,\mathrm{d}y\,\mathrm{d}z. \tag{18}$$

The membrane strain energy in the webs also comprises direct and shear strain energy contributions. The complete expressions for the direct strain in the more compressed and less compressed webs are very similar to those for the flanges presented in Eq. (15), thus:

$$\begin{aligned}\varepsilon_{z,\mathrm{wc}} &= \frac{\partial u_{\mathrm{t,wc}}}{\partial z} + \frac{\partial u_\mathrm{wc}}{\partial z} + \frac{1}{2}\left(\frac{\partial w_\mathrm{wc}}{\partial z}\right)^2 - \frac{1}{2}\left(\frac{\partial w_{\mathrm{wc}0}}{\partial z}\right)^2 - \Delta \\ &= -\left(q_t - q_{t0}\right)\frac{b\pi^2}{2L}\sin\frac{\pi z}{L} + \left\{g_{1\mathrm{wc}}\right\}_y \dot{u}_1 + \left\{g_{2\mathrm{wc}}\right\}_y \dot{u}_2 \\ &\quad + \frac{1}{2}\left\{f_{1\mathrm{wc}}^2\right\}_y \dot{w}_1^2 + \frac{1}{2}\left\{f_{2\mathrm{wc}}^2\right\}_y \left(\dot{w}_2^2 - \dot{w}_0^2\right) + \left\{f_{1\mathrm{wc}} f_{2\mathrm{wc}}\right\}_y \dot{w}_1 \dot{w}_2 - \Delta, \end{aligned} \tag{19}$$

$$\begin{aligned}\varepsilon_{z,\mathrm{wt}} &= \frac{\partial u_{\mathrm{t,wt}}}{\partial z} + \frac{\partial u_{\mathrm{wt}}}{\partial z} + \frac{1}{2}\left(\frac{\partial w_{\mathrm{wt}}}{\partial z}\right)^2 - \frac{1}{2}\left(\frac{\partial w_{\mathrm{wt0}}}{\partial z}\right)^2 - \Delta \\ &= (q_t - q_{t0})\,\frac{b\pi^2}{2L}\sin\frac{\pi z}{L} + \{g_{1\mathrm{wt}}\}_y\,\dot{u}_1 + \{g_{2\mathrm{wt}}\}_y\,\dot{u}_2 \\ &\quad + \frac{1}{2}\left\{f_{1\mathrm{wt}}^2\right\}_y\dot{w}_1^2 + \frac{1}{2}\left\{f_{2\mathrm{wt}}^2\right\}_y\left(\dot{w}_2^2 - \dot{w}_0^2\right) + \{f_{1\mathrm{wt}}f_{2\mathrm{wt}}\}_y\,\dot{w}_1\dot{w}_2 - \Delta.\end{aligned} \tag{20}$$

Unlike the flanges, the shear strains in the webs only contain the terms from the local mode due to their relatively small thickness, thus:

$$\begin{aligned}\gamma_{yz,\mathrm{wc}} &= \frac{\partial u_{\mathrm{wc}}}{\partial y} + \frac{\partial w_{\mathrm{wc}}}{\partial y}\frac{\partial w_{\mathrm{wc}}}{\partial z} - \frac{\partial w_{\mathrm{wc0}}}{\partial y}\frac{\partial w_{\mathrm{wc0}}}{\partial z} \\ &= \{g'_{1\mathrm{wc}}\}_y\,u_1 + \{g'_{2\mathrm{wc}}\}_y\,u_2 + \{f'_{1\mathrm{wc}}f_{1\mathrm{wc}}\}_y\,\dot{w}_1 w_1 \\ &\quad + \{f'_{2\mathrm{wc}}f_{2\mathrm{wc}}\}_y\,(\dot{w}_2 w_2 - \dot{w}_0 w_0) + \{f'_{1\mathrm{wc}}f_{2\mathrm{wc}}\}_y\,w_1\dot{w}_2 + \{f_{1\mathrm{wc}}f'_{2\mathrm{wc}}\}_y\,\dot{w}_1 w_2,\end{aligned} \tag{21}$$

$$\begin{aligned}\gamma_{yz,\mathrm{wt}} &= \frac{\partial u_{\mathrm{wt}}}{\partial y} + \frac{\partial w_{\mathrm{wt}}}{\partial y}\frac{\partial w_{\mathrm{wt}}}{\partial z} - \frac{\partial w_{\mathrm{wt0}}}{\partial y}\frac{\partial w_{\mathrm{wt0}}}{\partial z} \\ &= \{g'_{1\mathrm{wt}}\}_y\,u_1 + \{g'_{2\mathrm{wt}}\}_y\,u_2 + \{f'_{1\mathrm{wt}}f_{1\mathrm{wt}}\}_y\,\dot{w}_1 w_1 \\ &\quad + \{f'_{2\mathrm{wt}}f_{2\mathrm{wt}}\}_y\,(\dot{w}_2 w_2 - \dot{w}_0 w_0) + \{f'_{1\mathrm{wt}}f_{2\mathrm{wt}}\}_y\,w_1\dot{w}_2 + \{f_{1\mathrm{wt}}f'_{2\mathrm{wt}}\}_y\,\dot{w}_1 w_2.\end{aligned} \tag{22}$$

Again, assuming that $\varepsilon_{y,\mathrm{wc}} = -\nu\varepsilon_{z,\mathrm{wc}}$ and $\varepsilon_{y,\mathrm{wt}} = -\nu\varepsilon_{z,\mathrm{wt}}$, the membrane strain energy stored in both webs is given thus:

$$U_{\mathrm{m,w}} = \frac{1}{2}\int_0^L\int_{-d/2}^{d/2}\int_{-t_{\mathrm{w}}/2}^{t_{\mathrm{w}}/2}\left[E\left(\varepsilon_{z,\mathrm{wc}}^2 + \varepsilon_{z,\mathrm{wt}}^2\right) + G\left(\gamma_{yz,\mathrm{wc}}^2 + \gamma_{yz,\mathrm{wt}}^2\right)\right]\mathrm{d}x\,\mathrm{d}y\,\mathrm{d}z. \tag{23}$$

The total end-shortening $\mathcal{E}$ comprises terms from pure squash, the global sway mode and the local in-plane displacement. The expression for the work done by the external load is given by:

$$P\mathcal{E} = P\int_0^L\left[\Delta + \left(q_s^2 - q_{s0}^2\right)\frac{\pi^2}{2}\cos^2\frac{\pi z}{L} - \Delta_{\mathrm{m}}\right]\mathrm{d}z, \tag{24}$$

where:

$$\Delta_{\mathrm{m}} = \frac{\left(2\phi_{\mathrm{t}}\left\{g_{1\mathrm{f}}\right\}_x + \{g_{1\mathrm{wc}}\}_y + \{g_{1\mathrm{wt}}\}_y\right)\dot{u}_1 + \left(2\phi_{\mathrm{t}}\left\{g_{2\mathrm{f}}\right\}_x + \{g_{2\mathrm{wc}}\}_y + \{g_{2\mathrm{wt}}\}_y\right)\dot{u}_2}{2b(\phi_{\mathrm{t}} + \phi_{\mathrm{c}})}. \tag{25}$$

In summary, the total potential energy V can be expressed by the summation of all the strain energy terms minus the work done by the external load:

$$V = U_{\mathrm{b,o}} + U_{\mathrm{b,fl}} + U_{\mathrm{b,wcl}} + U_{\mathrm{b,wtl}} + U_{\mathrm{m,f}} + U_{\mathrm{m,w}} - P\mathcal{E}. \tag{26}$$

2.4. Variational formulation and eigenvalue analysis

The governing equations for equilibrium are obtained by performing the calculus of variations on the total potential energy V following the well established procedure presented in previous work [55, 16, 36, 37]. The integrand of the total potential energy V can be expressed as a Lagrangian ($\mathcal{L}$) of the form:

$$V = \int_0^L \mathcal{L}\left(\ddot{w}_i, \dot{w}_i, w_i, \dot{u}_i, u_i, z\right) \mathrm{d}z, \tag{27}$$

where $i = \{1, 2\}$. Equilibrium of the system requires that V is stationary for any small changes in w_i and u_i. Therefore, the governing equilibrium equations can be obtained by setting the first variation of V to zero:

$$\delta V = \int_0^L \left[\frac{\partial \mathcal{L}}{\partial \ddot{w}_i}\delta\ddot{w}_i + \frac{\partial \mathcal{L}}{\partial \dot{w}_i}\delta\dot{w}_i + \frac{\partial \mathcal{L}}{\partial w_i}\delta w_i + \frac{\partial \mathcal{L}}{\partial \dot{u}_i}\delta\dot{u}_i + \frac{\partial \mathcal{L}}{\partial u_i}\delta u_i\right] \mathrm{d}z = 0. \tag{28}$$

Since $\delta\ddot{w}_i = \mathrm{d}(\delta\dot{w}_i)/\mathrm{d}z$, $\delta\dot{w}_i = \mathrm{d}(\delta w_i)/\mathrm{d}z$ and $\delta\dot{u}_i = \mathrm{d}(\delta u_i)/\mathrm{d}z$, integration by parts allows the development of the Euler–Lagrange equations for w_i and u_i, which comprise a fourth order ordinary differential equation (ODE) for w_i and second order ODE for u_i, thus:

$$\frac{\mathrm{d}^2}{\mathrm{d}z^2}\left(\frac{\partial \mathcal{L}}{\partial \ddot{w}_i}\right) - \frac{\mathrm{d}}{\mathrm{d}z}\left(\frac{\partial \mathcal{L}}{\partial \dot{w}_i}\right) + \frac{\partial \mathcal{L}}{\partial w_i} = 0, \tag{29}$$

$$\frac{\mathrm{d}}{\mathrm{d}z}\left(\frac{\partial \mathcal{L}}{\partial \dot{u}_i}\right) - \frac{\partial \mathcal{L}}{\partial u_i} = 0. \tag{30}$$

Moreover, equilibrium also requires the minimization of V with respect to the generalized coordinates q_s, q_t and Δ, leading to three integral equations:

$$\frac{\partial V}{\partial q_s} = 0, \quad \frac{\partial V}{\partial q_t} = 0, \quad \frac{\partial V}{\partial \Delta} = 0. \tag{31}$$

The first expression in Eq. (31) provides a relationship between the global imperfection parameters q_{s0} and q_{t0} that is obtained by setting global mode amplitudes q_s and q_t, and local buckling mode functions, *i.e.* u_i, w_i and their derivatives with respect to z, to zero:

$$q_{s0} = (1 + s)\, q_{t0}, \tag{32}$$

where s is the shear correction factor, thus:

$$s = \frac{\pi^2 E b^2}{4GL^2}\left(\frac{1}{3} + \frac{\phi_\mathrm{c}}{\phi_\mathrm{t}}\right). \tag{33}$$

It should be mentioned that the corresponding relationship, $q_s = (1 + s)q_t$, also applies before local buckling is triggered [37].

The boundary conditions for w_i, u_i and their derivatives are for simply-supported conditions at $z = 0$ and for symmetry conditions at $z = L/2$:

$$w_i(0) = \ddot{w}_i(0) = \dot{w}_i(L/2) = \dddot{w}_i(L/2) = u_i(L/2) = 0. \tag{34}$$

Two further boundary conditions can be obtained from the variational formulation with regards to the in-plane displacements u_i, hence:

$$\left[\frac{\partial \mathcal{L}}{\partial \dot{u}_i}\delta u_i\right]_0^L = 0. \tag{35}$$

Linear eigenvalue analysis for the perfect strut is conducted to determine the global buckling load $P_{\mathrm{o}}^{\mathrm{C}}$. This is evaluated by considering the condition where the Hessian matrix $\mathbf{V}_{ij}$ is singular, where $q_s = q_t = 0$ and $w_1 = w_2 = u_1 = u_2 = 0$:

$$\det\left(\mathbf{V}_{ij}\right) = \begin{vmatrix} \frac{\partial^2 V}{\partial q_s^2} & \frac{\partial^2 V}{\partial q_s \partial q_t} \\ \frac{\partial^2 V}{\partial q_t \partial q_s} & \frac{\partial^2 V}{\partial q_t^2} \end{vmatrix} = 0. \tag{36}$$

Solving Eq. (36) gives the following expression:

$$P_{\mathrm{o}}^{\mathrm{C}} = \frac{2\pi^2 E I_{\mathrm{w}}}{L^2} + \frac{\pi^2 E t_{\mathrm{f}} b^3}{2\left(1+s\right)L^2}\left(\frac{1}{3} + \frac{\phi_{\mathrm{c}}}{\phi_{\mathrm{t}}}\right). \tag{37}$$

Note that if Euler–Bernoulli bending theory had been assumed, the shear modulus $G \to \infty$ and hence $s \to 0$, then $P_{\mathrm{o}}^{\mathrm{C}}$ would reduce to the classical Euler buckling load, as would be expected.

3. Numerical results, verification and discussion

Previous studies on the imperfection sensitivity of thin-walled struts [5, 18, 23, 24, 56] found that the maximum erosion in the load-carrying capacity principally occurs within the range where the global buckling load is close to the local buckling load, *i.e.* the transitional range between zones 1 and 2 and the whole range of zone 2, as shown schematically in Figure 6. Therefore, the imperfection sensitivity of two typical length struts, where global and local buckling are critical respectively but the ratio of the global and local buckling loads is close to unity in both cases, are analysed in detail. The cross-section geometry and material properties of the example struts are presented in Table 1 with Table 2 summarizing the strut lengths, the buckling loads and corresponding zones, as defined in [37]. The effects of global imperfections, local imperfections and their combination on the nonlinear equilibrium path and load-carrying capacity of the two example struts are investigated. Since the complete system of the nonlinear coupled ordinary differential equations is too complicated to be solved analytically, the solution is obtained within the powerful numerical continuation and bifurcation software AUTO-07P [38]. The software has been shown in previous studies [13, 57, 55, 44, 23, 36, 37] to be capable of solving

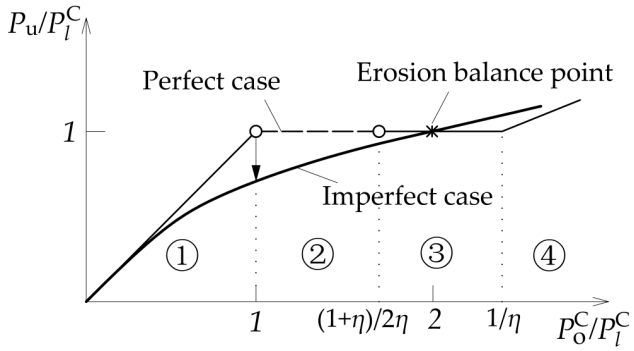

Figure 6: The van der Neut curve for the geometrically perfect and imperfect cases [5]. The quantity η is the stiffness reduction factor due to the local buckling of the flanges; P_u, P_o^C and P_l^C are the ultimate, the global buckling and the local buckling loads respectively. The imperfect case line shows that within zones 1–3, there is a reduced ultimate load compared to the perfect case. There is also an 'erosion balance point' marked where the curve for the imperfect case intersects with the perfect case.

Table 1: Cross-section geometry and material properties of the rectangular hollow section struts in the numerical examples.

Flange width b	60 mm
Web depth d	120 mm
Flange thickness t_f	1 mm
Web thickness t_w	1 mm
Young's Modulus E	210 kN/mm^2
Poisson's ratio ν	0.3

coupled nonlinear differential equations subject to boundary and integral conditions, and importantly, tracing the evolution of solutions with varying system parameters, which in the present case are the nonlinear equilibrium paths. Moreover, it has the key capability of finding and classifying different kinds of bifurcation points and switching between, as well as tracing, different solution branches.

Typical equilibrium paths for perfect and imperfect example struts alongside the numerical continuation procedures to solve the equilibrium paths using AUTO are shown diagrammatically in Figure 7. For the case where only the global imperfection exists two stages are required to obtain the whole equilibrium path, as shown in Figure 7(a–b). Branch switching is necessary at the pitchfork bifurcation point (B) [58], which is the generic term for a conventional symmetric (stable or unstable) bifurcation [6], where local and hence

Table 2: Theoretical values of the global and local buckling loads for the two separate lengths studied.

L (mm)	P_o^C (kN)	$P_{\mathrm{l,AUTO}}^\mathrm{C}$ (kN)	$P_{\mathrm{l,ABAQUS}}^\mathrm{C}$ (kN)	$P_\mathrm{o}^\mathrm{C}/P_\mathrm{l}^\mathrm{C}$	Zone	Length description
4800	22.67	24.61	24.57	0.92	1	'Long'
4500	25.79	24.61	24.58	1.05	2	'Transitional'

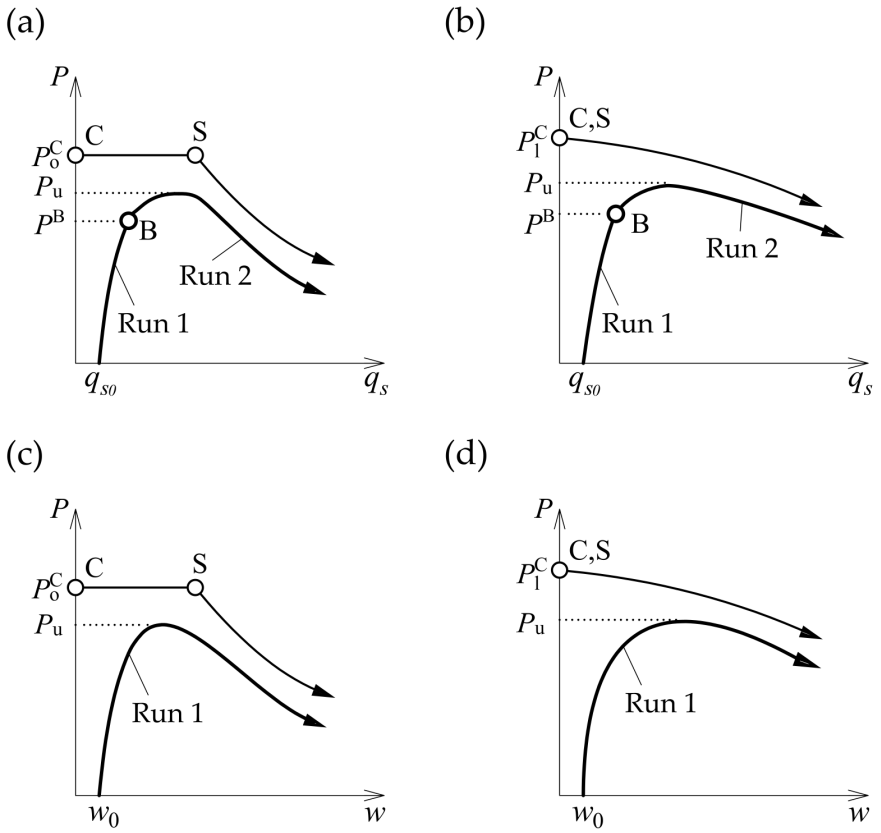

Figure 7: Sketches of the equilibrium paths and their numerical continuation procedures in AUTO for the imperfect struts primarily in zones 1 and 2. (a) Global buckling being critical with an initial out-of-straightness global imperfection q_{s0} only; (b) local buckling being critical with q_{s0} only; (c) global buckling being critical with a mono-symmetric local imperfection w_0 only or with both w_0 and q_{s0}; (d) local buckling being critical with w_0 only or with both w_0 and q_{s0}. The thicker and thinner lines represent the imperfect and perfect systems respectively. Circles represent critical (C) and secondary (S) bifurcation points for the perfect systems and a pitchfork bifurcation point (B) for the imperfect system; $P_{\rm o}^{\rm C}$, $P_{\rm l}^{\rm C}$, $P^{\rm B}$ and $P_{\rm u}$ represent the global buckling load, the local buckling load, the load at the pitchfork bifurcation point and the ultimate load respectively.

interactive buckling is triggered, to trace the post-buckling equilibrium path. For the cases with pure local imperfections and with combined local and global imperfections, only one run is required to obtain the whole equilibrium path, as shown in Figure 7(c, d). The mono-symmetric local imperfection immediately breaks the symmetry as the numerical run begins and therefore q_s and q_t are introduced without the need for branch switching.

3.1. Global imperfections ($q_{s0} \neq 0$, $w_0 = 0$)

In this section, the effects of a purely global imperfection are studied. Only initial sway and tilt imperfections, *i.e.* q_{s0} and q_{t0}, which satisfy the relationship from Eq. (32), are introduced. A set of values for the normalized initial sway imperfection amplitude q_{s0} ranging from 10^{-4} to 10^{-3} is selected for analysis. Figures 8 and 9 show a family of equilibrium paths with increasing global imperfection size and the relationship between the ultimate load and the global imperfection amplitude for the long (zone 1) and transitional length (zone 2) struts respectively. It is clearly observed that the ultimate load decreases as the imperfection size increases. For $q_{s0} = 1/1000$, which is the tolerance level for global imperfections recommended in the relevant part of Eurocode 3 [11], the erosion in the load-carrying capacity is approximately 25% compared with the critical buckling load of the perfect system for both struts. From the equilibrium path, the transition from highly unstable to approximately neutral post-buckling behaviour can be observed with the increase of the global imperfection size q_{s0}. Specifically, the snap-back and the sharp load drop at the secondary bifurcation in the load–end-shortening relationship for the perfect case disappear gradually with the increase of the imperfection size. It can also be seen that all equilibrium paths converge asymptotically to the same state, as would be expected from classical studies [6].

Moreover, for the perfect case and the cases where the imperfection size is vanishingly small, the triggering of local buckling represents the ultimate state, which is followed by unstable post-buckling behaviour. However, with increasing imperfection size, there is a further increase in the load-carrying capacity after local buckling in the more compressed web is triggered, as shown in Figures 8 and 9, which has also been reported previously [5, 59, 60, 25]. Therefore, it would seem that determining the load at the pitchfork bifurcation point P^{B} would provide a safe, yet accurate, method to predict the ultimate load for struts with purely global imperfections.

As shown in Figure 10(a) and (c), the global imperfection size also affects the profile of the interactive buckling mode in the proximity of the pitchfork bifurcation point. For the long length strut, the interactive buckling mode becomes more localized with increasing imperfection size. As for the transitional length strut, the global imperfection immediately breaks the symmetry, making the profile change from approximately periodically distributed along the length to localized at mid-span. The increasing imperfection size also increases the degree of localization of the interactive buckling mode as that for the long length strut. It should be noted that in both cases the increase in the degree of localization is accompanied by a reduction in the wavelength. With the progress of mode interaction, the post-buckling mode spreads towards the boundary and becomes distributed along the whole length of the strut, as shown in Figure 10(b, d). It can be concluded that, in a

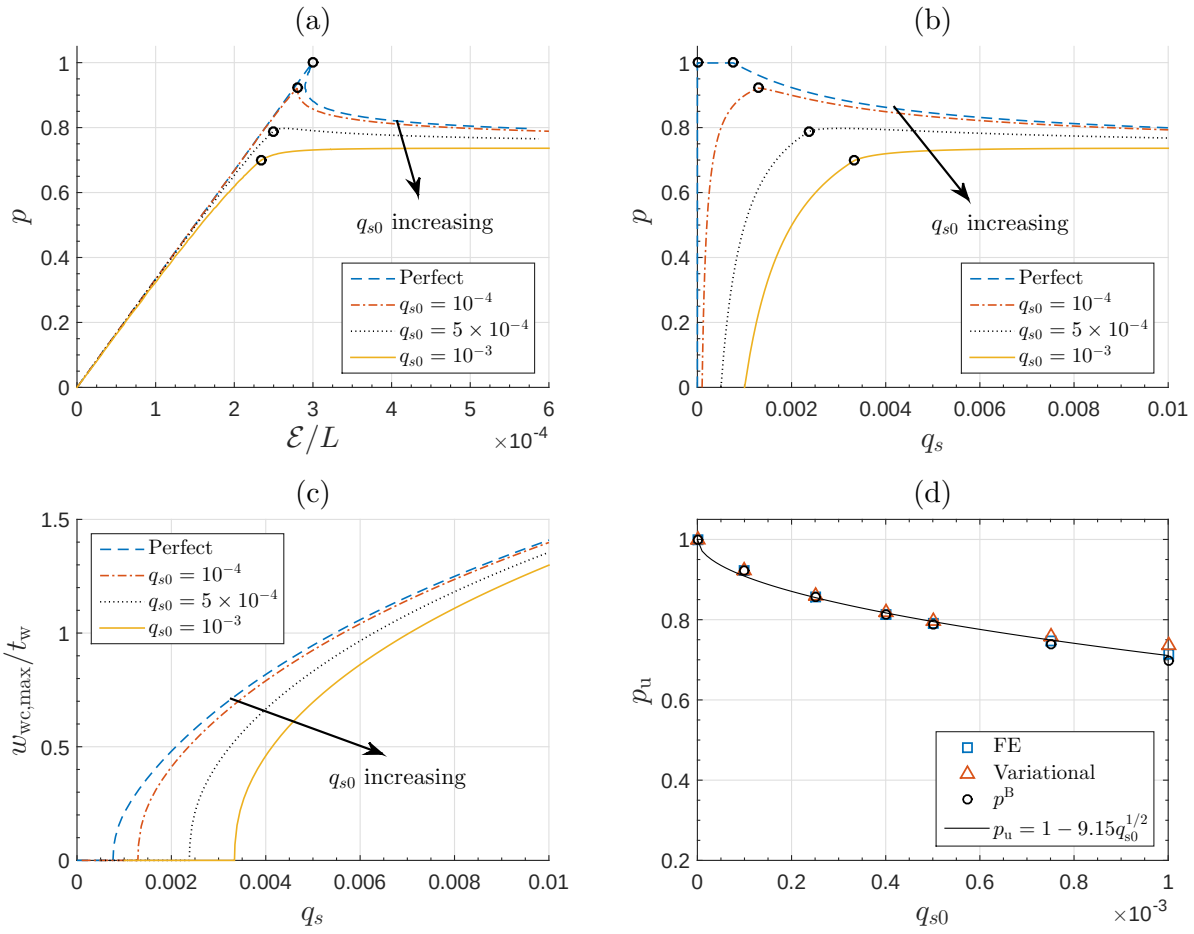

Figure 8: Equilibrium paths and the imperfection sensitivity graph for the long length strut ($L = 4.8\,\mathrm{m}$) with different global imperfection sizes q_{s0}. Graphs of the normalized load ratio $p = P/P^{\mathrm{C}}$, where P^{C} is the critical buckling load for the perfect strut, versus (a) the normalized end-shortening $\mathcal{E}/L$, and (b) the normalized amplitude of the sway mode q_s; (c) shows the normalized maximum amplitude of the local buckling deflection in the more compressed web $w_{\mathrm{wc,max}}/t_{\mathrm{w}}$ versus q_s; (d) shows the normalized ultimate load $p_{\mathrm{u}} = P_{\mathrm{u}}/P^{\mathrm{C}}$ from both the FE and variational models and the normalized load at the pitchfork bifurcation point for the imperfect system $p^{\mathrm{B}} = P^{\mathrm{B}}/P^{\mathrm{C}}$ against q_{s0} showing the sensitivity to initial global imperfections. Circles in (a) and (b) represent bifurcation points.

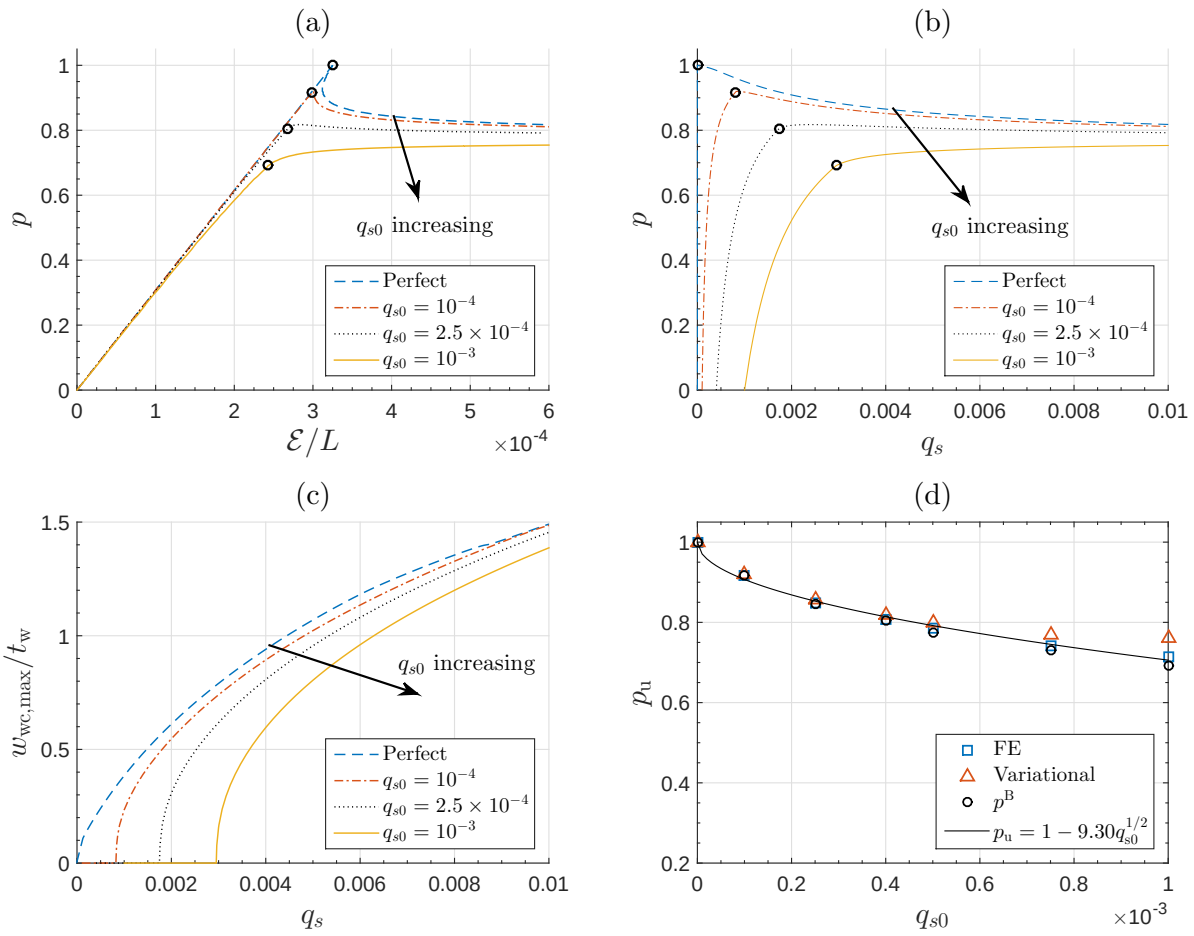

Figure 9: Equilibrium paths and the imperfection sensitivity graph for the transitional length strut ($L = 4.5\,\mathrm{m}$) with different global imperfection sizes q_{s0}. Graphs (a)–(d) are as described in Figure 8.

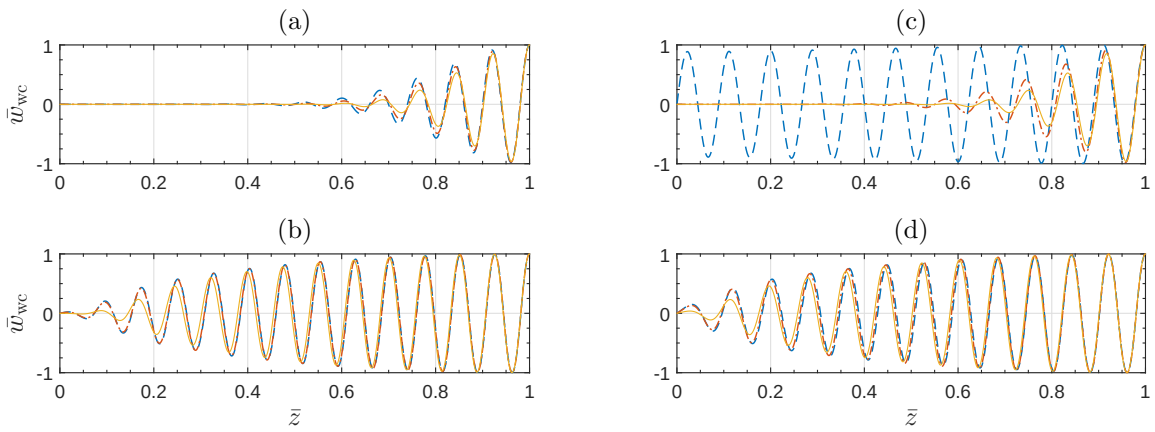

Figure 10: Numerical solutions of the longitudinal profile of the local out-of-plane displacement in the more compressed web $\bar{w}_{\mathrm{wc}} = w_{\mathrm{wc}}/w_{\mathrm{wc}}(\bar{z} = 1)$ at (a, c) the pitchfork bifurcation point and (b, d) where $q_s = 8 \times 10^{-3}$ for the long length strut (a–b) and the transitional length strut (c–d) respectively. The dashed, dot-dashed and solid lines represent the cases with perfect and imperfect ($q_{s0} = 10^{-4}$ and 10^{-3}) geometries respectively. Note that the longitudinal coordinate is normalized with respect to half of the strut length $\bar{z} = 2z/L$.

similar way to the equilibrium path, the post-buckling mode also converges approximately to the same profile in the far-field post-buckling range.

3.2. Local imperfections ($w_0 \neq 0$, $q_{s0} = 0$)

For the study where only local imperfections exist, the global imperfection parameters q_{s0} and q_{t0} are set to zero. The cross-section profile of the local imperfection is assumed to be mono-symmetric and defined by Eqs. (5)–(7). The longitudinal component of the local imperfection w_0 is determined based on fitting the longitudinal component of the first local buckling mode from the FE models using Eq. (10). The profile of the imperfection is shown in Figure 11. For the long length strut, it is determined that $\alpha = 4.314$ and $\beta = 47$; whereas for the transitional length strut, $\alpha = 5$ and $\beta = 47$. A set of values for the normalized local imperfection amplitude A_0/t_{w} ranging from 0.01 to 0.6 is selected for analysis.

Figures 12 and 13 show a family of equilibrium paths with increasing local imperfection size and the relationship between the ultimate load and the local imperfection amplitude for the long and transitional length struts respectively. The ultimate load drops substantially with increasing local imperfection amplitude. For $A_0/t_{\mathrm{w}} = 0.6 = d/(200t_{\mathrm{w}})$, which is the tolerance level for local imperfections recommended in Eurocode 3 [11], the erosion in the load-carrying capacity is greater than 20% compared with the perfect case for both struts considered. As for the equilibrium paths, in a similar way to the global imperfection case, a transition from highly unstable to mildly stable behaviour is observed in both struts with increasing local imperfection size. Specifically, for the perfect case and the cases where the imperfection size is vanishingly small, reaching the ultimate load is

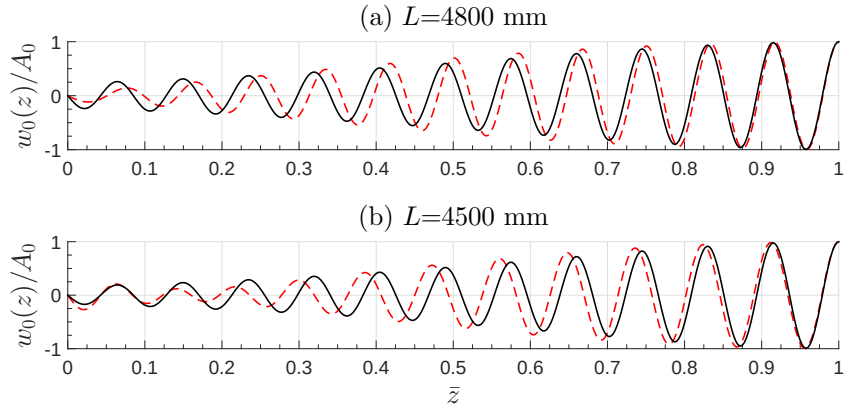

Figure 11: Longitudinal component of initial local imperfections for (a) the long length strut and (b) the transitional length strut. Solid and dashed lines represent fitting functions and the first local buckling mode from FE respectively. Note that the longitudinal coordinate is defined as in Figure 10.

accompanied by potentially unstable behaviour, *i.e.* snap-backs in the load–end-shortening relationship and a simultaneous sharp load drop may be expected. However, for the cases with larger imperfection sizes, the behaviour is relatively stable, *i.e.* the stiffness decreases with increase of the applied load but remains positive and the deformation level at the ultimate load is relatively large.

It should be noted that there is a snap-back in the q_s–$w_{\mathrm{wc}}/t_{\mathrm{w}}$ relationship for the long length strut with a normalized local imperfection amplitude $A_0/t_{\mathrm{w}} = 0.01$, as shown in Figure 12(c). It corresponds to a jump in the local mode, as shown in Figure 14. Before the mode jump occurs at $q_s = 0.002$, the number of peaks and troughs in the form of w_{wc} with $A_0/t_{\mathrm{w}} = 0.01$ is the same as that for the strut with $A_0/t_{\mathrm{w}} = 0.14$, which is determined by the pre-defined local imperfection function, as shown in Figures 11(a) and 14(a). However, after the mode jump, there are more peaks and troughs for the strut with $A_0/t_{\mathrm{w}} = 0.01$ and the number is the same as that for the perfect case, as shown in Figure 14(b); this finding is also in accord with previous studies [23, 24]. With increasing local imperfection size, the formation of new peaks or troughs requires more membrane strain energy, which would necessitate a longer snap-back path. This, perhaps, explains why no mode jump is observed for the cases with larger imperfection sizes in the current deformation range, *i.e.* where $q_s < 10^{-2}$. It should also be noted that the mode jumping phenomenon is not observed in the transitional length strut with the same imperfection size ($A_0/t_{\mathrm{w}} = 0.01$) before $q_s = 10^{-2}$, which in fact occurs at $q_s = 1.2 \times 10^{-2}$. This may, in turn, be explained by the fact that local buckling is critical in that case and the local mode defined by the imperfection is well developed, thus requiring an excessive amount of strain energy (and hence a longer snap-back path) to trigger any jump in the post-buckling mode.

3.3. Combined imperfections ($q_{s0} \neq 0$, $w_0 \neq 0$)

The effects of combining local and global imperfections are now studied. As mentioned earlier, according to Eurocode 3 [11, 32], the tolerance levels for global and local imper-

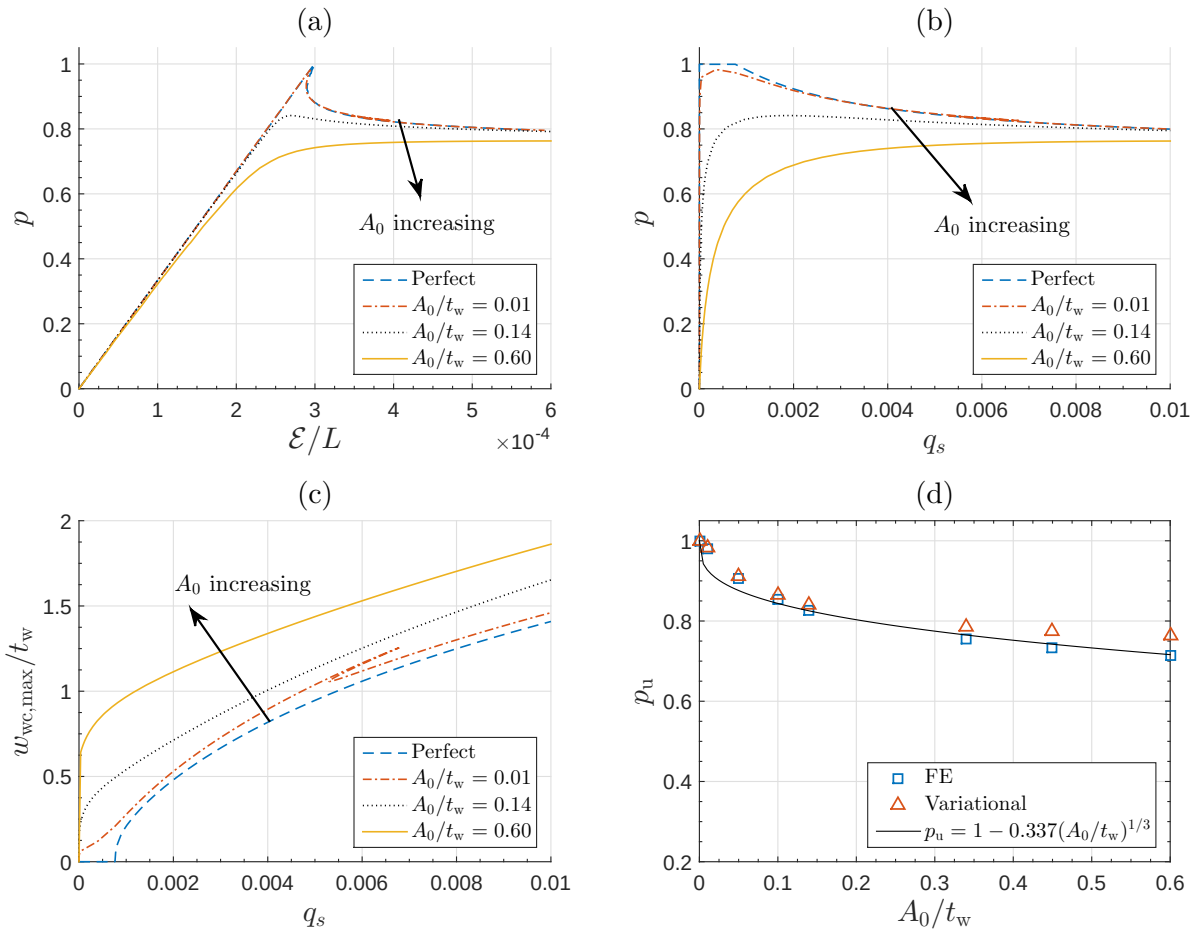

Figure 12: Equilibrium paths and the imperfection sensitivity graph for the long length strut with different local imperfection amplitudes A_0. Graphs (a–c) are as described in Figure 8. Graph (d) shows the normalized ultimate load p_u from both FE and variational models against A_0 showing the sensitivity to initial local imperfections.

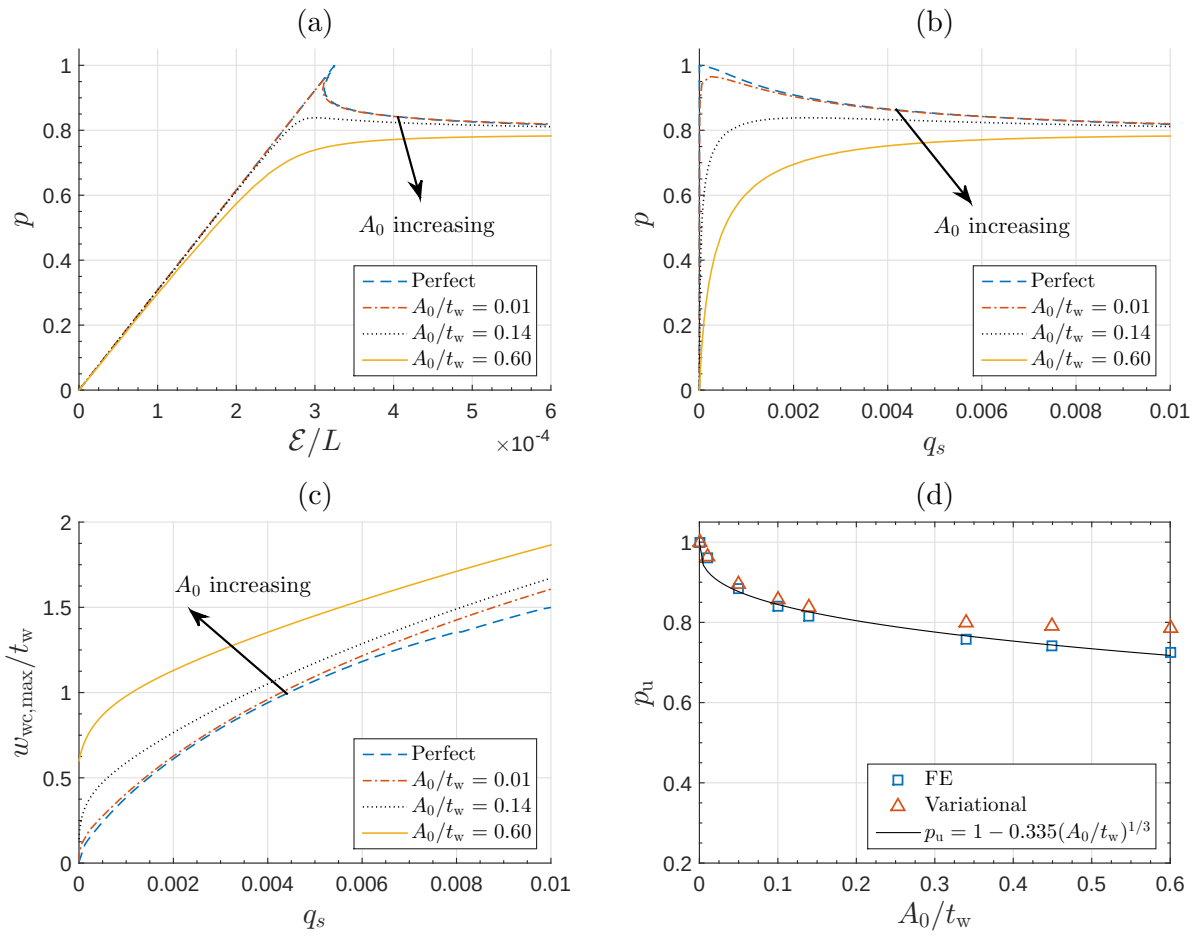

Figure 13: Equilibrium paths and the imperfection sensitivity graph for the transitional length strut with different local imperfection amplitudes A_0. Graphs (a)–(d) are as described in Figure 12.

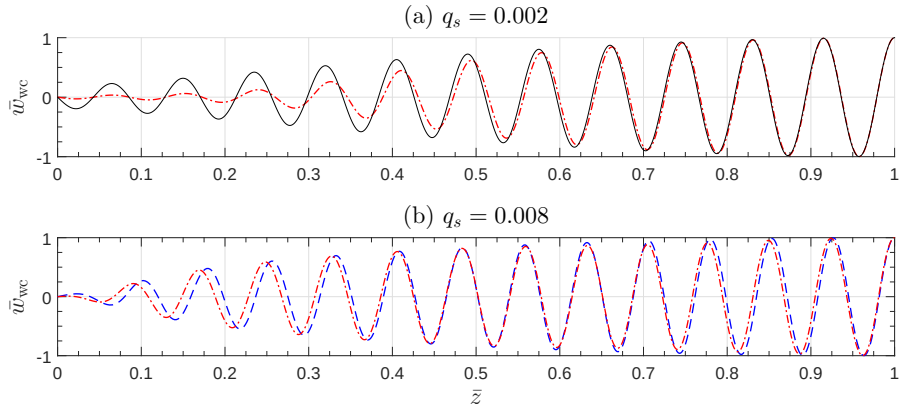

Figure 14: Evolution of the numerical solutions for the normalized local out-of-plane displacement in the more compressed web where (a) $q_s = 0.002$ and (b) $q_s = 0.008$ for the long length strut with different local imperfection amplitudes A_0. The solid, dot-dashed and dashed lines represent where $A_0/t_{\mathrm{w}} = 0.14$, $A_0/t_{\mathrm{w}} = 0.01$ and the perfect case respectively.

fections are $q_{\mathrm{s0,tol}}L = L/1000$ and $A_{0,\mathrm{tol}} = d/200$ respectively. Hence, the imperfection combination selected currently is set to be proportional to and also normalized with respect to this combination, which is defined as $\mathbf{W}_{\mathcal{E}0} = \bar{W}_{\mathcal{E}0}\{q_{\mathrm{s0,tol}}L, A_{0,\mathrm{tol}}\}$, where $\bar{W}_{\mathcal{E}0}$ is a non-dimensional scaling factor.

Figures 15 and 16 show the nonlinear equilibrium paths and the imperfection sensitivity relationship for both example struts. With increasing imperfection size, a transition from highly unstable to mildly stable behaviour is also observed. It should be noted that there remains a snap-back in the relationship between the local and global mode amplitudes for the long length strut with $\bar{W}_{\mathcal{E}0} = 1/60$, where the global and local imperfection amplitudes are $L/60000$ and $d/12000$ respectively; this implies that there is a jump in the local mode.

Moreover, compared with purely global or local imperfection cases, the introduction of the other imperfection-type leads to a further 10% load drop. For the imperfections at the Eurocode 3 tolerance levels ($\bar{W}_{\mathcal{E}0} = 1$), the load-carrying capacity erosion in comparison with the perfect case is over 30% for both struts. According to the definition suggested by Gioncu [7], this may be classified as a strong interaction. A larger load-carrying capacity erosion would be expected for the cases where $P_{\mathrm{o}}^{\mathrm{C}}/P_{\mathrm{l}}^{\mathrm{C}}$ is approximately unity.

3.4. Verification and discussion

For verification purposes, nonlinear FE models of the example struts with the same material and geometric properties and geometric imperfections as the variational model were developed in the commercial FE package ABAQUS [40] using the four-noded, reduced-integration S4R shell elements. Two different methods were adopted to model the geometric imperfections in the FE models: the first one used the keyword '*IMPERFECTION' to introduce the shape of eigenmodes from linear buckling analysis, which is very straightforward; the second one used MATLAB [61] to generate the nodal coordinates input file for

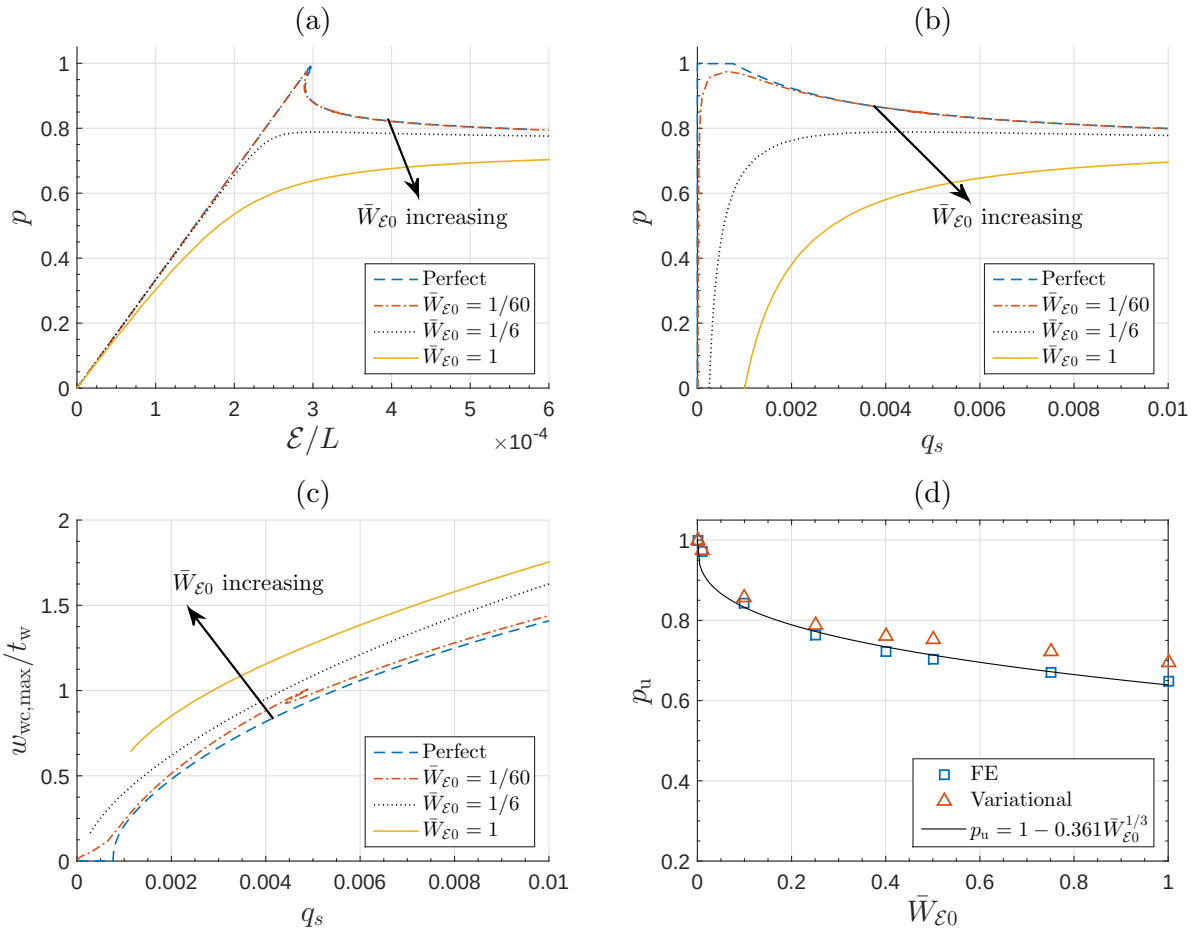

Figure 15: Equilibrium paths and the imperfection sensitivity graph for the long length strut with different normalized combined imperfection sizes $\bar{W}_{\mathcal{E}0}$. Graphs (a)–(c) are as described in Figure 8. Graph (d) shows the normalized ultimate load p_{u} from both the FE and variational models against $\bar{W}_{\mathcal{E}0}$ showing the sensitivity to the combined local and global imperfections. Note that $\bar{W}_{\mathcal{E}0} = 1$ corresponds to the global imperfection amplitude $q_{s0}L$ being $L/1000$ and the local imperfection amplitude A_0 being $d/200$.

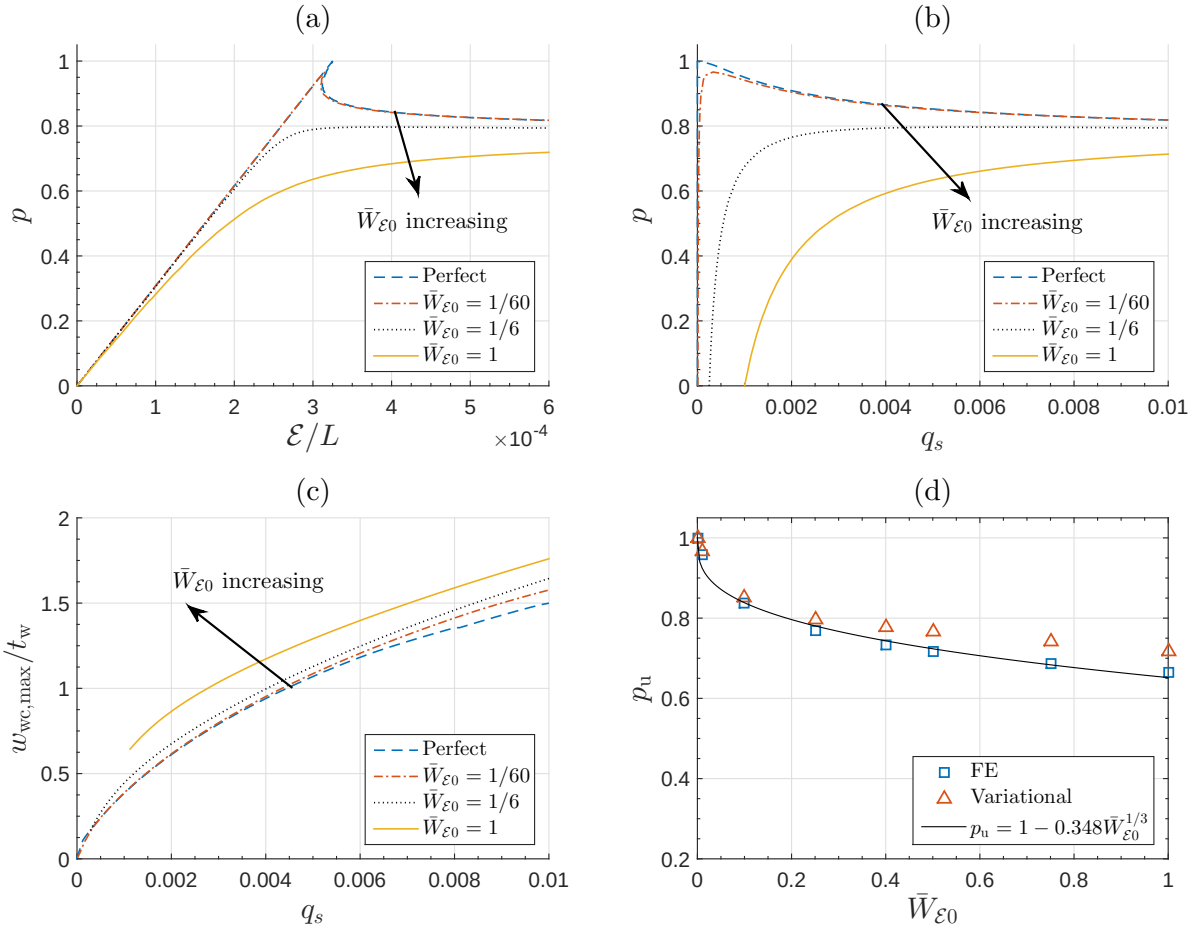

Figure 16: Equilibrium paths and the imperfection sensitivity graph for the transitional length strut with different normalized combined imperfection sizes $\bar{W}_{\mathcal{E}0}$. Graphs (a)–(d) are as described in Figure 15.

the FE model with pre-defined global and local imperfections from Eqs. (8) and (9) respectively, which can model more general imperfection cases. For the pure global imperfection case and the perfect case, the first method was adopted to introduce the imperfection or the necessary geometric perturbation to simulate the post-buckling response of the perfect case; the second method was used in the cases where local imperfections were introduced either with or without the global imperfection.

Owing to the discontinuous pitchfork bifurcation response at the initial instability, it was not possible to analyse the interactive post-buckling behaviour of the cases, where only global imperfections or only symmetric local imperfections exist, in ABAQUS directly, unless imperfections existed naturally from the discretization. Therefore, an initial perturbation in the geometry was introduced to transform the discontinuous bifurcation problem into a continuous one [62]. In the current study, the eigenmode shapes from linear buckling analysis were adopted as the profiles for the initial local or global geometric perturbations

and the scale factors for the local and global perturbations were set to $10^{-3}t_{\mathrm{w}}$ and $10^{-6}L$ respectively. These were sufficiently small sizes to ensure that the response essentially mimicked the perfect cases as far as possible, without encountering the pitchfork bifurcations that would have led to convergence problems. As for the nonlinear solution, the Riks arclength method [39] was adopted to trace the nonlinear equilibrium path. The full modelling details, such as meshing size, convergence control, and boundary conditions, can be found in [36].

The comparison of the ultimate load from the FE and the variational models are shown in (d) of Figures 8–9, 12–13, 15–16 (inclusive). The results from the variational models generally show good comparisons with those from the FE models, with the variational models generally predicting slightly higher ultimate loads. The discrepancy increases with increasing imperfection size and the maximum relative difference $(P_{\mathrm{u}} - P_{\mathrm{u,FE}})/P_{\mathrm{u,FE}}$, which occurs at the tolerance imperfection combination case ($\bar{W}_{\mathcal{E}0} = 1$) for the transitional length strut, is slightly below 8%.

The reasons for the stiffer response or higher ultimate load prediction of the variational model for the perfect case have been discussed thoroughly in [37] and also apply currently. Firstly, when the more compressed web buckles, the neutral axis for strut flexure would move to the less compressed side, thus introducing an additional bending moment to the strut. The effect becomes more significant with the progression of interactive post-buckling, which facilitates the load reaching the ultimate value and subsequently dropping. In order to consider this effect, an additional displacement function would need to be introduced in the current model to describe the movement of the neutral axis. Secondly, in the current formulation, it is assumed that the effect of local buckling on the transverse stress in each plate is negligible, which leads to the relationship $\varepsilon_x = -\nu\varepsilon_z$ in the flanges and $\varepsilon_y = -\nu\varepsilon_z$ in the webs. In fact, this assumption is valid only when the local out-of-plane displacement of the plate is small. In the advanced post-buckling range, the assumption would be no longer valid, as demonstrated in Figure 17. The assumption also simplifies the transverse displacement field, *i.e.* the in-plane displacement field across the cross-section [37], which may lead to a 'locking' problem (essentially, a stiffer response), as reported by a recent study [63]. Moreover, the in-plane cross-section displacement would also reduce the effective flexural rigidity of the strut. To resolve the problem, an independent local mode to describe the transverse in-plane displacement field in both flanges and webs would be required, but this would complicate the variational model considerably.

Thirdly, in the current formulation, the cross-section component of the direct in-plane displacement field is assumed to be the same as that of the out-of-plane one. Although this assumption satisfies the kinematic boundary conditions, it does not represent the actual cross-sectional displacement field very well. To describe the cross-section component of the direct in-plane displacement field better, the solutions from classical theory [47] could be adopted with the introduction of more functions to describe the variation of the cross-section component along the strut length. However, the current model accuracy suggests that any advantage would be minor and be mostly offset by the additional model complexity. Finally, the cross-section profile of the local mode is assumed to remain unchanged along the length of the strut and also throughout the progression of mode interaction, and

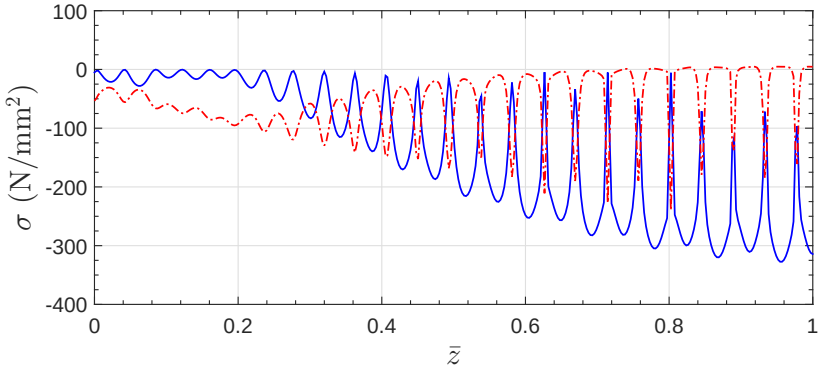

Figure 17: Membrane stress distributions along the strut corner line of the more compressed web at the ultimate load from FE for the transitional length strut with the tolerance imperfection combination ($\bar{W}_{\mathcal{E}0}$=1). Solid and dot-dashed lines represent the longitudinal and transverse stresses respectively, showing that the transverse stresses are definitely not zero.

the only variable is the modal amplitude, as can be seen in Eq. (2). However, the profile is affected by the ratio of axial force and bending moment, which varies along the length and also throughout the entire loading history. Furthermore, some higher order effects, such as those discussed in [37], would also affect the cross-section profile. All of these factors taken together lead to the stiffer response of the variational model, thus overestimating the ultimate load especially in the cases where the imperfection size is close to the recommended tolerance levels within the Eurocode. However, the errors are within generally acceptable bounds and the variational model does provide a better insight into the system mechanics.

Based on the FE results, curves have been fitted to describe the ultimate load–normalized imperfection size relationship, as shown in (d) of Figures 8–9, 12–13, 15–16 (inclusive). For the pure global imperfection case, the expressions for both example struts indicate approximately a 1/2 power law relationship; for the pure local imperfection and combined imperfection cases, the expressions for both example struts indicate approximately a 1/3 power law relationship, which is also observed in I-section struts susceptible to mode interaction [64]. Moreover, the transitional length strut exhibits relatively more sensitivity to global imperfections and the long length strut exhibits relatively more sensitivity to pure local and combined imperfections.

4. Variational model application and parametric study

4.1. Simplified method to predict load at pitchfork bifurcation ($q_{s0} \neq 0$, $w_0 = 0$)

From the numerical results hitherto, it was demonstrated that for the case where only a global imperfection exists, the load at the pitchfork bifurcation point P^{B} can be used to predict the ultimate load with relatively good accuracy and be safe, as shown in Figures 8(d) and 9(d). Therefore, a simplified method to predict P^{B} is proposed based on the method developed in previous work [36], which determined the local buckling load of the

more compressed web undergoing global buckling and the corresponding global buckling amplitude at the secondary bifurcation point for perfect thin-walled rectangular section struts exhibiting global–local mode interaction.

Equation (31) provides the governing equation for the relationship between q_s, q_t and P along the equilibrium path. By setting the terms related to the local mode to be zero, the first two expressions of Eq. (31) can be written as:

$$\frac{\partial V}{\partial q_s} = \pi^2 G t_{\mathrm{f}} b L \left[(q_s - q_t) - (q_{s0} - q_{t0}) \right] + \frac{\pi^4 E I_{\mathrm{w}} (q_s - q_{s0})}{L} - P \frac{\pi^2 L q_s}{2} = 0, \tag{38}$$

$$\frac{\partial V}{\partial q_t} = \frac{\pi^4 E t_{\mathrm{f}} b^3}{4L} \left(\frac{1}{3} + \frac{\phi_{\mathrm{c}}}{\phi_{\mathrm{t}}} \right) (q_t - q_{t0}) - \pi^2 G t_{\mathrm{f}} b L \left[(q_s - q_t) - (q_{s0} - q_{t0}) \right] = 0. \tag{39}$$

Substituting Eq. (39) into Eq. (38) to remove the shear term and using the relationship in Eq. (32) gives the following expression:

$$P = P_{\mathrm{o}}^{\mathrm{C}} \left(\frac{q_s - q_{s0}}{q_s} \right). \tag{40}$$

If no local buckling occurs, P would increase with q_s and tend towards $P_{\mathrm{o}}^{\mathrm{C}}$ in the limit.

However, the bending stiffness would drop due to local buckling in the more compressed web and flanges. Since the transverse stress component is neglected currently, the direct stress in the more compressed web σ_{wc} before local buckling occurs can be written thus:

$$\sigma_{\mathrm{wc}} = E \varepsilon_{\mathrm{wc}} = - \frac{\pi^2 E b (q_t - q_{t0})}{2L} \sin \frac{\pi z}{L} - \frac{P}{A_{\mathrm{g}}}, \tag{41}$$

where $A_{\mathrm{g}} = 2(b t_{\mathrm{f}} + d t_{\mathrm{w}})$ is the gross cross-sectional area. From the numerical results shown in Figures 10(a, c), the local mode is initially localized. Instead of analysing the whole web with the entire strut length, it was demonstrated in [36] that when σ_{wc} at mid-span reaches the local buckling stress of the more compressed web $\sigma_{\mathrm{wc}}^{\mathrm{C}}$, interactive buckling can be assumed to have been triggered. The expression for the local buckling stress of the more compressed web element restrained by both flanges is given by:

$$\sigma_{\mathrm{wc}}^{\mathrm{C}} = \frac{k_{\mathrm{p}} \pi^2 E}{12(1 - \nu^2)(d/t_{\mathrm{w}})^2} \tag{42}$$

and the complete expression for the plate buckling coefficient k_{p} may be found in [36]. For the practically significant case where the cross-section has a uniform wall thickness ($\phi_{\mathrm{t}} = 1$), the expression for k_{p} was determined to be thus:

$$k_{\mathrm{p}} = 4.33 + 0.76 \phi_{\mathrm{c}} - 0.1 \phi_{\mathrm{c}}^2. \tag{43}$$

By substituting Eqs. (32) and (40) into Eq. (41), the relationship between P^{B} and the

global imperfection size q_{s0} is obtained:

$$P^{\mathrm{B}} = \frac{A_{\mathrm{g}}}{2}\left[\frac{\pi^2 E b q_{s0}}{2(1+s)L} + \frac{P_{\mathrm{o}}^{\mathrm{C}}}{A_{\mathrm{g}}} + \sigma_{\mathrm{wc}}^{\mathrm{C}} - \sqrt{\left(\frac{P_{\mathrm{o}}^{\mathrm{C}}}{A_{\mathrm{g}}} - \sigma_{\mathrm{wc}}^{\mathrm{C}}\right)^2 + \frac{\pi^2 E b q_{s0}}{2(1+s)L}\left(\frac{\pi^2 E b q_{s0}}{2(1+s)L} + \frac{2P_{\mathrm{o}}^{\mathrm{C}}}{A_{\mathrm{g}}} + 2\sigma_{\mathrm{wc}}^{\mathrm{C}}\right)}\right]. \tag{44}$$

Figure 18 shows the comparison of the normalized load $p^{\mathrm{B}} = P^{\mathrm{B}}/P^{\mathrm{C}}$ obtained from Eq.

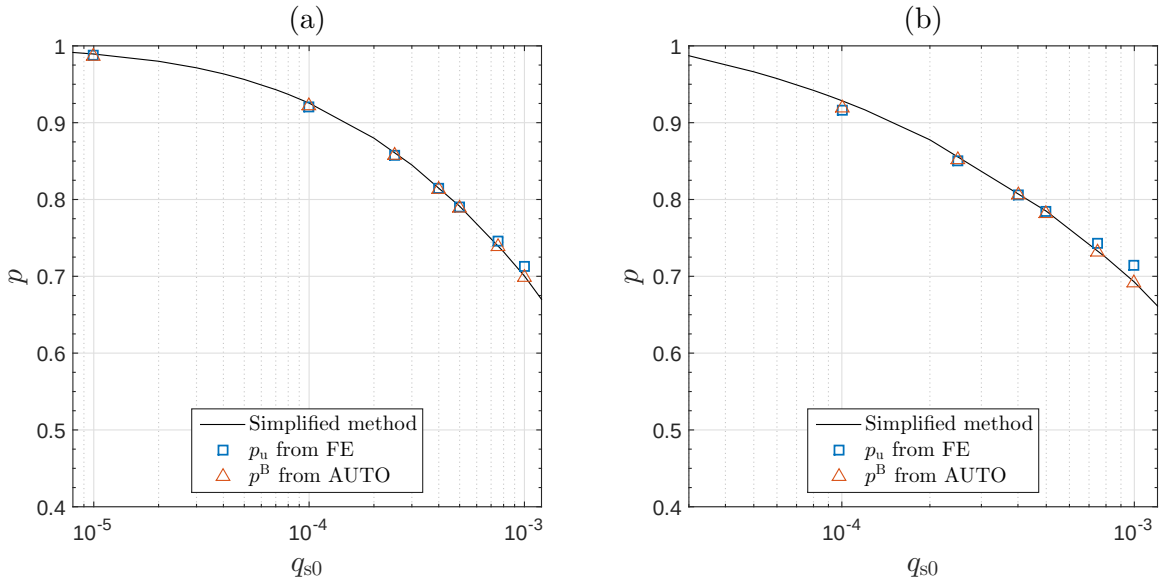

Figure 18: Comparison of the normalized load p^{B} using the simplified method and the full variational model against the normalized ultimate load p_{u} from the FE models for (a) the long length strut and (b) the transitional length strut. Note that only global imperfections are included in both example struts.

(44) and the full variational model against the normalized ultimate load $p_{\mathrm{u}} = P_{\mathrm{u}}/P^{\mathrm{C}}$ from the FE model for example struts with purely global imperfections for different imperfection sizes. For the long length strut, the simplified method shows excellent comparisons with the full variational model for P^{B}, as shown in Figure 18(a). For the transitional length strut, the comparison is good for the cases where the global imperfection size is larger than 10^{-4}. For tiny global imperfections, the simplified method would overestimate P^{B}. This is caused by the fact that when the imperfection size is vanishingly small, the system would behave very similarly to the perfect system, *i.e.* the less compressed web would also buckle [37] and therefore the restraints on the more compressed web would be smaller, which leads to a smaller value of k_{p}. In general, for the current two example struts, the simplified method provides a safe, yet accurate prediction of the ultimate load for different imperfection sizes. Finally, it should be mentioned that if the material yield stress f_{y} replaced $\sigma_{\mathrm{wc}}^{\mathrm{C}}$ in Eq. (44), the equation would revert to the classical Perry–Robertson formula [12] for the failure load of an imperfect column.

4.2. Simplified method to predict the ultimate load ($q_{s0} = 10^{-3}$, $w_0 = 0$)

Figure 19 presents the relationship between the ultimate and pitchfork bifurcation loads for different length struts with tolerance level global imperfections ($q_{s0} = 10^{-3}$). In the

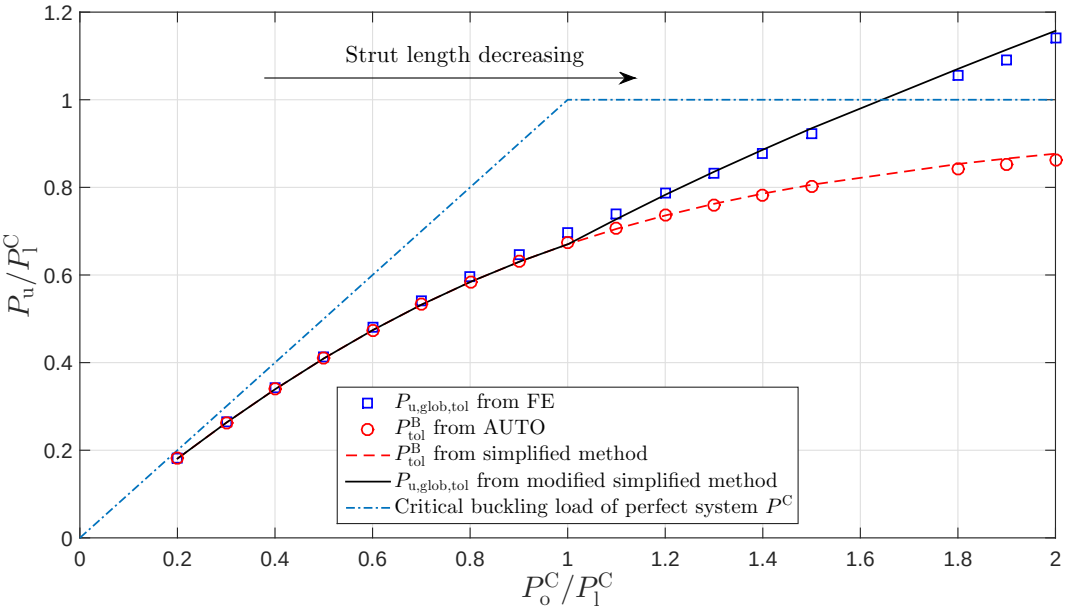

Figure 19: Length effects on the ultimate and pitchfork bifurcation load of thin-walled RHS struts with purely tolerance level global imperfections ($q_{s0} = 10^{-3}$). Note that the cross-section and material properties of the struts are presented in Table 1.

range where global buckling is critical ($P^{\mathrm{C}}_{\mathrm{o}}/P^{\mathrm{C}}_{\mathrm{l}} < 1$), the ultimate load is approximately the same as the pitchfork bifurcation load. Therefore, Eq. (44) can be used as an accurate prediction of the ultimate load for such cases. However, in the range where local buckling is critical, the pitchfork bifurcation load is significantly smaller than the ultimate load and the difference increases with decreasing strut length, which implies that the triggering of local–global mode interaction in such cases does not lead to unstable post-buckling behaviour.

The prerequisite of the simplified method for predicting the ultimate load is that the effective global buckling load $\Phi_{\mathrm{r}} P^{\mathrm{C}}_{\mathrm{o}}$ is less than or very close to P^{B}, where Φ_{r} is the bending stiffness reduction factor due to local buckling of the more compressed web and flanges [37]. Otherwise, the load would still increase beyond P^{B} with a reduced stiffness and would tend to $\Phi_{\mathrm{r}} P^{\mathrm{C}}_{\mathrm{o}}$, even though mode interaction is triggered, as shown in Figures 8 and 9. Therefore, more calibration parameters could be introduced in Eq. (44) to fit it for the whole length range. An equation is proposed based on the FE results in the range where $P^{\mathrm{C}}_{\mathrm{o}}/P^{\mathrm{C}}_{\mathrm{l}} \leqslant 4$:

$$P_{\mathrm{u,glob,tol}} = \begin{cases} P^{\mathrm{B}}_{\mathrm{tol}} & \text{for } P^{\mathrm{C}}_{\mathrm{o}}/P^{\mathrm{C}}_{\mathrm{l}} \leqslant 1, \\ P^{\mathrm{B}}_{\mathrm{tol}} \left[0.32 \left(P^{\mathrm{C}}_{\mathrm{o}}/P^{\mathrm{C}}_{\mathrm{l}} - 1\right) + 1\right] & \text{for } 1 < P^{\mathrm{C}}_{\mathrm{o}}/P^{\mathrm{C}}_{\mathrm{l}} \leqslant 4. \end{cases} \tag{45}$$

The average ratio of Eq. (45) to $P_{\mathrm{u,FE,glob,tol}}$ is 0.998 and the coefficient of variation (COV) is 0.96%, which represents an excellent fit. However, it should be noted that the equation is only valid for the current geometric parameter space; an extensive parametric study on geometric properties, *i.e.* plate width–thickness ratio and cross-section aspect ratio, would be required to make the equation more generic and this is currently being undertaken.

4.3. Simplified method to predict the ultimate load ($q_{s0} = 10^{-3}$, $A_0 = d/200$)

In this subsection, the ultimate load for thin-walled RHS struts with purely tolerance level local imperfections, purely tolerance level global imperfections and their combinations for different length struts is investigated. The aim is to establish the relationship between the ultimate load for the cases with purely tolerance level global imperfections and those with tolerance level combined imperfections alongside calibrating Eq. (45) to be valid for the latter cases.

Figure 20(a) shows the ultimate load for thin-walled RHS struts with purely tolerance level local imperfections, purely tolerance level global imperfections and their combinations in the range: $P_{\mathrm{o}}^{\mathrm{C}}/P_{\mathrm{l}}^{\mathrm{C}}$=[0.2, 2.0]. It can be observed that the struts exhibit sensitivity to

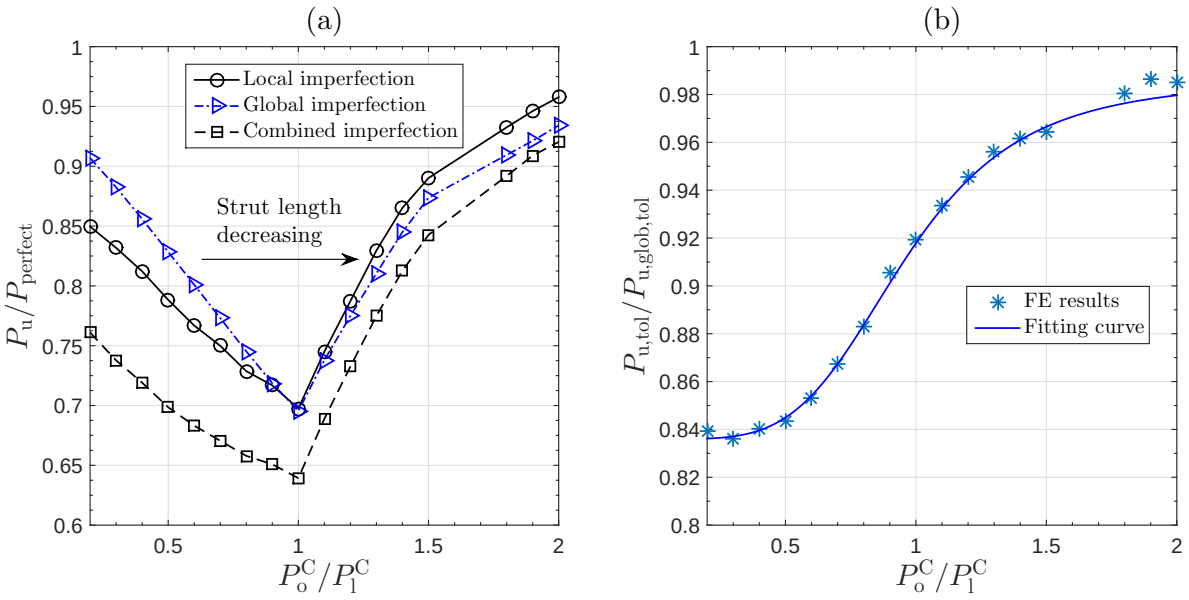

Figure 20: (a) Effects of tolerance level local imperfections, global imperfections and their combination on the ultimate load for thin-walled RHS struts with different lengths. (b) Ratio of $P_{\mathrm{u,tol}}$ to $P_{\mathrm{u,glob,tol}}$ versus the strut length, where $P_{\mathrm{u,tol}}$ and $P_{\mathrm{u,glob,tol}}$ represent the ultimate load with tolerance level combined imperfections and tolerance level global imperfections respectively. Note that material and cross-section properties are presented in Table 1. Local imperfection profiles are affine to the lowest local buckling mode from linear buckling analysis using FE models.

both local and global imperfections and the load erosion is most significant at the point where $P_{\mathrm{o}}^{\mathrm{C}}/P_{\mathrm{l}}^{\mathrm{C}}$=1. For the current example struts with the cross-section properties as presented in Table 1 and the imperfection tolerance level (A_0/t=0.6 and q_{s0}=10^{-3}) selected,

the ultimate load erosion due to purely tolerance level local and global imperfections is nearly equal at the point where $P_{\mathrm{o}}^{\mathrm{C}}/P_{\mathrm{l}}^{\mathrm{C}}$=1. Therefore, an opportunity to determine the relative significance of both imperfection types on the ultimate load erosion for different length ranges is provided. The principal finding from Figure 20(a) is that the ultimate load with purely local imperfections is lower than that with purely global imperfections in the range where global buckling is critical and vice versa. This observation implies that struts where global buckling is critical are more sensitive to local imperfections than global imperfections and vice versa.

The underlying mechanism of the critical buckling mode dependent imperfection sensitivity may be explained based on the interactive buckling behaviour of perfect systems. No matter to which type the critical buckling mode belongs, the failure of perfect thin-walled RHS struts is controlled by the symmetry breaking action of mode interaction [65, 37]. In the perfect case or the case with imperfections purely in the shape of the primary buckling mode, the secondary buckling mode would be triggered when the primary mode is fully developed. Since the primary mode is stable or neutral, the imperfect system would approximate to the perfect case in the purely elastic scenarios. The imperfections with interactive post-buckling mode profiles would have an immediate destabilization effect on the system, *i.e.* a reduction in stiffness, which would facilitate the triggering of the secondary mode and expedite the reaching of the ultimate state [65].

As for the effects of superposing a tolerance level global imperfection on a local imperfection, the ratio of the ultimate load for struts with purely tolerance level local imperfections to that of struts with combined imperfections, $P_{\mathrm{u,loc,tol}}/P_{\mathrm{u,tol}}$, almost remains constant in the range where global buckling is critical, with the average and the COV being 0.896 and 1.2% respectively. It should be noted that the value is very close to the strength reduction factor 0.877 of the nominal strength for slender elastic columns from the current Direct Strength Method (DSM) [66]. In the range where local buckling is critical, $P_{\mathrm{u,loc,tol}}/P_{\mathrm{u,tol}}$ increases with increasing $P_{\mathrm{o}}^{\mathrm{C}}/P_{\mathrm{l}}^{\mathrm{C}}$, with $P_{\mathrm{u,loc,tol}}/P_{\mathrm{u,tol}}$=0.965 at $P_{\mathrm{o}}^{\mathrm{C}}/P_{\mathrm{l}}^{\mathrm{C}}$=2. The ratio remains approximately constant beyond the point. As for the effects of superposing a tolerance level local imperfection on struts with a tolerance level global imperfection, $P_{\mathrm{u,glob,tol}}/P_{\mathrm{u,tol}}$ increases with the increasing $P_{\mathrm{o}}^{\mathrm{C}}/P_{\mathrm{l}}^{\mathrm{C}}$ from 0.839 at $P_{\mathrm{o}}^{\mathrm{C}}/P_{\mathrm{l}}^{\mathrm{C}}$=0.2 to 0.985 at $P_{\mathrm{o}}^{\mathrm{C}}/P_{\mathrm{l}}^{\mathrm{C}}$=2, as shown in Figure 20(b), and the ratio converges gradually to unity beyond this point.

As shown in Figure 20(b), a curve is fitted based on the numerical results to describe the relationship between $P_{\mathrm{u,tol}}$ and $P_{\mathrm{u,glob,tol}}$:

$$P_{\mathrm{u,tol}} = \left[0.836 + \frac{0.18}{1.2 + \left(P_{\mathrm{o}}^{\mathrm{C}}/P_{\mathrm{l}}^{\mathrm{C}}\right)^{-4.24}}\right] P_{\mathrm{u,glob,tol}}. \tag{46}$$

The average ratio of Eq. (46) to FE results in the range $P_{\mathrm{o}}^{\mathrm{C}}/P_{\mathrm{l}}^{\mathrm{C}}$=[0.2, 4] is 1.000 and the COV is 0.63%. In a similar way to Eq. (45), the current equation is also limited to the current geometric space and further parametric studies are necessary to validate it for a wider range of cases.

4.4. Comparison with current design guidelines

In current design guidelines, the effective width method [67] and the Direct Strength Method (DSM) [66] can be used to consider the effects of local–global mode interaction on the ultimate strength. Owing to its relative simplicity, the DSM is used as the reference for the current parametric study on length, where the actual load-carrying capacity for struts susceptible to mode interaction is evaluated using the following expression:

$$\frac{P_{\mathrm{nl}}}{P_{\mathrm{ne}}} = \begin{cases} 1 & \text{for } \bar{\lambda}_{\mathrm{l}} \leq 0.776, \\ \left[1 - 0.15\left(P_{\mathrm{l}}^{\mathrm{C}}/P_{\mathrm{ne}}\right)^{0.4}\right]\left(P_{\mathrm{l}}^{\mathrm{C}}/P_{\mathrm{ne}}\right)^{0.4} & \text{for } \bar{\lambda}_{\mathrm{l}} > 0.776, \end{cases} \tag{47}$$

where P_{nl} and P_{ne} are the nominal axial strengths for local and global buckling respectively, and the local slenderness $\bar{\lambda}_{\mathrm{l}} = \sqrt{P_{\mathrm{ne}}/P_{\mathrm{l}}^{\mathrm{C}}}$ with $P_{\mathrm{l}}^{\mathrm{C}}$ being the critical elastic local buckling load. Moreover, P_{ne} is defined thus:

$$\frac{P_{\mathrm{ne}}}{P_{\mathrm{y}}} = \begin{cases} 0.658^{\bar{\lambda}_{\mathrm{o}}^2} & \text{for } \bar{\lambda}_{\mathrm{o}} \leq 1.5, \\ 0.877/\bar{\lambda}_{\mathrm{o}}^2 & \text{for } \bar{\lambda}_{\mathrm{o}} > 1.5. \end{cases} \tag{48}$$

Here, the global slenderness $\bar{\lambda}_{\mathrm{o}} = \sqrt{P_{\mathrm{y}}/P_{\mathrm{o}}^{\mathrm{C}}}$, the squash load of the gross cross-section $P_{\mathrm{y}} = A_{\mathrm{g}} f_{\mathrm{y}}$ and $P_{\mathrm{o}}^{\mathrm{C}}$ is the elastic critical buckling load for either flexural, torsional, or flexural–torsional buckling. Currently, since globally slender geometries are being considered, *i.e.* $\bar{\lambda}_{\mathrm{o}} > 1.5$, P_{ne} can be expressed as:

$$P_{\mathrm{ne}} = 0.877 P_{\mathrm{o}}^{\mathrm{C}}. \tag{49}$$

As can be seen from Eq. (47), a calibration exponent, which is a function of the ratio of $P_{\mathrm{l}}^{\mathrm{C}}$ and P_{ne}, is introduced to consider the effects of mode interaction in the imperfection sensitive zone. By substituting Eq. (49) into Eq. (47), the strength curve for struts, with cross-section and material properties given in Table 1, is presented in Figure 21. The imperfection sensitivity zone due to local–global interactive buckling suggested by the DSM for the current case is $0.687 < P_{\mathrm{o}}^{\mathrm{C}}/P_{\mathrm{l}}^{\mathrm{C}} < 1.455$, where the upper bound is the erosion balance point, as defined in Figure 6. The maximum load erosion occurs at $P_{\mathrm{o}}^{\mathrm{C}}/P_{\mathrm{l}}^{\mathrm{C}} = 1$ and is found to be 22.2%.

However, from the previous section, the load erosion due to the tolerance imperfection at the 'naive optimum' point, where $P_{\mathrm{o}}^{\mathrm{C}}/P_{\mathrm{l}}^{\mathrm{C}} = 1$, is approximately 40%, as shown in Figure 21. Therefore, a parametric study on strut length using the verified variational and the FE models is conducted to show the ultimate load erosion at different lengths and identify the 'imperfection sensitive' zone, thus checking the validity of the DSM for such cases. As shown in Figure 21, the ultimate loads predicted by the verified variational and the FE models are significantly lower than those predicted by the DSM. Moreover, the erosion balance point also moves from zone 3 to zone 4. The range of the 'imperfection sensitive' zone in zone 1, where global buckling is critical, is also much wider than that suggested by the DSM. Therefore, a refined DSM-style equation based on fitting the FE

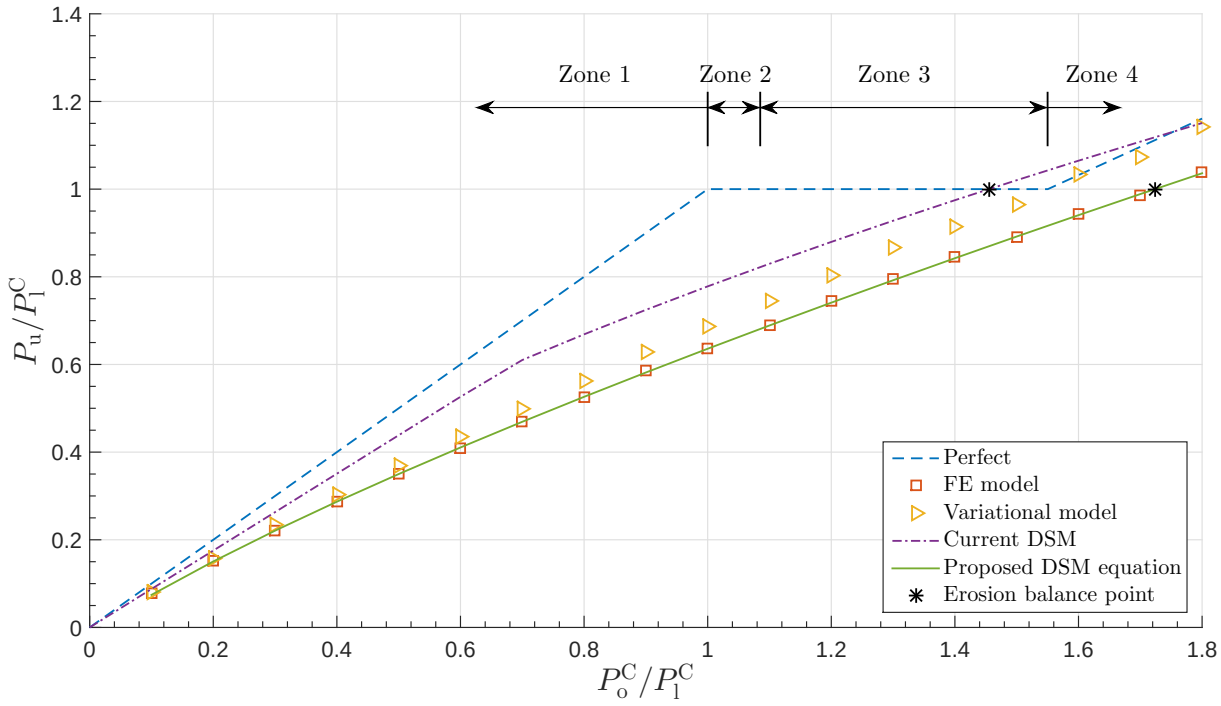

Figure 21: Numerically obtained van der Neut curve for perfect and imperfect struts with cross-section and material properties presented in Table 1 and tolerance level geometric imperfection sizes recommended by EC3 [11]. Strength predictions using current and proposed DSM equations are also plotted.

results is proposed:

$$\frac{P_{\mathrm{nl}}}{P_{\mathrm{ne}}} = \left[1 - 0.29\left(\frac{P_{\mathrm{l}}^{\mathrm{C}}}{P_{\mathrm{ne}}}\right)^{0.275}\right]\left(\frac{P_{\mathrm{l}}^{\mathrm{C}}}{P_{\mathrm{ne}}}\right)^{0.275}. \tag{50}$$

The mean value of the ratio of the ultimate load from Eq. (50) and the FE models in the current length range is 0.994 and the coefficient of variation is 1.46%. It should be strongly emphasized that Eq. (50) is only valid for the current geometric parameter space. A more extensive parametric study is essential to make the new equation valid for much larger geometric parameter spaces. Moreover, the lower bound for the imperfection sensitivity zone due to local–global interactive buckling for the current example struts is tiny, *i.e.* $P_{\mathrm{o}}^{\mathrm{C}}/P_{\mathrm{l}}^{\mathrm{C}} < 0.01$, which is much smaller than that defined by the current DSM. This may be attributed from the global and local imperfection size adopted in the current study. As shown in Figure 22, the value of $P_{\mathrm{o}}^{\mathrm{C}}/P_{\mathrm{l}}^{\mathrm{C}}$ at the point where the effects of local–global mode interaction can be neglected, *i.e.* P_{u}=0.877$P_{\mathrm{o}}^{\mathrm{C}}$, decreases with the increasing imperfection size. In particular, it is very sensitive to the local imperfection size. Therefore, the lower boundary is not given in the current equation and will be the subject of further research. Finally, it should also be stressed that the errors between the results from the variational and the FE models increase marginally with the increasing value of $P_{\mathrm{o}}^{\mathrm{C}}/P_{\mathrm{l}}^{\mathrm{C}}$, *i.e.* with the

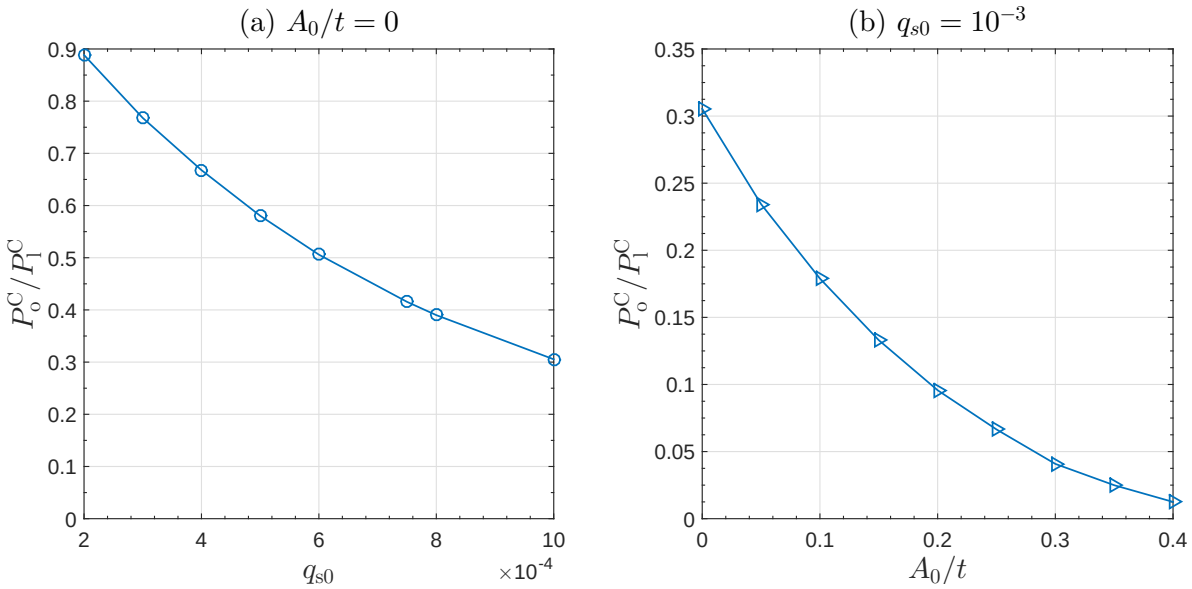

Figure 22: Locus of P_o^C/P_1^C at the lower bound of the imperfection sensitivity zone defined where $P_u = 0.877P_o^C$ versus (a) the global imperfection size without any local imperfection and (b) the local imperfection superposed with the global imperfection where q_{s0}=10^{-3}.

strut length decreasing; for instance, at $P_o^C/P_1^C = 1.8$, the ratio of the ultimate loads determined from the variational and the FE models is approximately 1.099.

5. Concluding remarks

A nonlinear variational model for axially-loaded thin-walled rectangular hollow section struts with initial global and local geometric imperfections has been developed using analytical techniques. Numerical examples, focusing on cases where the global buckling load is close to the local buckling load, have been presented and verified using the FE package ABAQUS. The sensitivity of two example struts exhibiting mode interaction to initial geometric imperfections has been quantified. With the increase of the geometric imperfection size, a transition from highly unstable to neutrally or mildly stable post-buckling behaviour is observed. A progressive change in the local buckling mode is identified in terms of both wavelength and amplitude. In particular, mode jumping within the interactive buckling mode, *i.e.* the change in the number of troughs and peaks of the local mode and snap-backs in the equilibrium path, is also observed in the cases where the local imperfection size is vanishingly small. A simplified method to predict the load at the pitchfork bifurcation point, where interactive buckling is triggered, is proposed for struts with purely global imperfections based on the verified variational model; it is demonstrated to be simple, yet safe and accurate for the cases studied.

A parametric study on the effects of global tolerance imperfections, local tolerance imperfections and their combinations on the ultimate load for struts with different lengths

was conducted. It was revealed that for struts with tolerance level global imperfections, the post-buckling behaviour after the pitchfork bifurcation point is unstable and stable for struts with global buckling and local buckling being critical respectively. It was also found that local imperfections are more significant than global imperfections for struts with global buckling being critical and global imperfections are more significant for struts with local buckling being critical. This is attributed to the characteristic behaviour where the alternative imperfection type would facilitate the necessary symmetry breaking to trigger interactive buckling. Based on the parametric study results, the simplified method to predict the pitchfork bifurcation load is calibrated to calculate the ultimate load for struts with tolerance level global and combined imperfections. A parametric study on strut length demonstrated the potential dangers of making unsafe predictions of actual load-carrying capacity by using the current guidelines of the Direct Strength Method (DSM). Therefore, a refined DSM equation has been proposed based on the present results.

Further research is being conducted to study the post-buckling behaviour and ultimate load-carrying capacity of perfect and imperfect struts exhibiting mode interaction in much wider geometric parameter spaces, *i.e.* different cross-section aspect ratios, plate width–thickness ratios and strut lengths. Moreover, the effects of material nonlinearity are also being investigated. The ultimate goal of the work is to provide robust design guidance on thin-walled rectangular hollow section struts susceptible to mode interaction for industrial practice.

Acknowledgment

Financial support for Jiajia Shen was provided by the President's PhD Scholarship scheme from Imperial College London.

References

[1] F. Bleich, Buckling strength of metal structures, McGraw-Hill, New York, 1952.

[2] S. P. Timoshenko, J. M. Gere, Theory of elastic stability, McGraw-Hill, New York, 1961.

[3] D. O. Brush, B. O. Almroth, Buckling of bars, plates, and shells, McGraw Hill, 1975.

[4] Z. P. Bažant, L. Cedolin, Stability of structures: Elastic, inelastic, fracture and damage theories, World Scientific, 2010.

[5] A. van der Neut, The interaction of local buckling and column failure of thin-walled compression members, in: Proceedings of the 12th International Congress on Applied Mechanics, Springer, 1969, pp. 389–399.

[6] J. M. T. Thompson, G. W. Hunt, A general theory of elastic stability, Wiley, London, 1973.

[7] V. Gioncu, General theory of coupled instabilities, Thin-Walled Struct. 19 (2) (1994) 81–127.

[8] E. Barbero, J. Tomblin, A phenomenological design equation for FRP columns with interaction between local and global buckling, Thin-Walled Struct. 18 (2) (1994) 117–131.

[9] J. Becque, K. J. R. Rasmussen, Experimental investigation of the interaction of local and overall buckling of stainless steel I-columns, ASCE J. Struct. Eng. 135 (11) (2009) 1340–1348.

[10] J. Becque, K. J. R. Rasmussen, Numerical investigation of the interaction of local and overall buckling of stainless steel I-columns, ASCE J. Struct. Eng. 135 (11) (2009) 1349–1356.

[11] EN-1993-1-3:2006E, Eurocode 3: Design of steel structures part 1-3. General rules-Supplementary rules for cold-formed members and sheeting (2006).

[12] N. S. Trahair, M. A. Bradford, D. Nethercot, L. Gardner, The behaviour and design of steel structures to EC3, CRC Press, 2007.

[13] G. W. Hunt, M. A. Wadee, Localization and mode interaction in sandwich structures, Proc. R. Soc. A 454 (1972) (1998) 1197–1216.

[14] M. A. Wadee, S. Yiatros, M. Theofanous, Comparative studies of localized buckling in sandwich struts with different core bending models, Int. J. Non-Linear Mech. 45 (2) (2010) 111–120.

[15] M. A. Wadee, M. Farsi, Cellular buckling in stiffened plates, Proc. R. Soc. A 470 (2168) (2014) 20140094.

[16] M. A. Wadee, L. Bai, Cellular buckling in I-section struts, Thin-Walled Struct. 81 (2014) 89–100.

[17] E. L. Liu, M. A. Wadee, Interactively induced localization in thin-walled I-section struts buckling about the strong axis, Structures 4 (2015) 13–26.

[18] W. T. Koiter, M. Pignataro, An alternative approach to the interaction between local and overall buckling in stiffened panels, in: B. Budiansky (Ed.), Buckling of Structures, International Union of Theoretical and Applied Mechanics, Springer Berlin Heidelberg, 1976, pp. 133–148.

[19] J. M. T. Thompson, J. D. Tulk, A. C. Walker, An experimental study of imperfection-sensitivity in the interactive buckling of stiffened plates, in: B. Budiansky (Ed.), Buckling of Structures, International Union of Theoretical and Applied Mechanics, Springer Berlin Heidelberg, 1976, pp. 149–159.

[20] J. Loughlan, The ultimate load sensitivity of lipped channel columns to column axis imperfection, Thin-Walled Struct. 1 (1) (1983) 75–96.

[21] P. Goltermann, H. Møllmann, Interactive buckling in thin-walled beams: II. Applications, Int. J. Solids Struct. 25 (7) (1989) 729–749.

[22] M. A. Wadee, Effects of periodic and localized imperfections on struts on nonlinear foundations and compression sandwich panels, Int. J. Solids Struct. 37 (8) (2000) 1191–1209.

[23] L. Bai, M. A. Wadee, Imperfection sensitivity of thin-walled I-section struts susceptible to cellular buckling, Int. J. Mech. Sci. 104 (2015) 162–173.

[24] M. A. Wadee, M. Farsi, Imperfection sensitivity and geometric effects in stiffened plates susceptible to cellular buckling, Structures 3 (2015) 172–186.

[25] E. L. Liu, M. A. Wadee, Mode interaction in perfect and imperfect thin-walled I-section struts susceptible to global buckling about the strong axis, Thin-Walled Struct. 106 (2016) 228–243.

[26] T. Graves Smith, The effect of initial imperfections on the strength of thin-walled box columns, Int. J. Mech. Sci. 13 (11) (1971) 911–925.

[27] J. Loughlan, N. Yidris, P. Cunningham, The effects of local buckling and material yielding on the axial stiffness and failure of uniformly compressed I-section and box-section struts, Thin-Walled Struct. 49 (2) (2011) 264–279.

[28] R. Maquoi, C. Massonnet, Interaction between local plate buckling and overall buckling in thin-walled compression members – theories and experiments, in: B. Budiansky (Ed.), Buckling of Structures, International Union of Theoretical and Applied Mechanics, Springer Berlin Heidelberg, 1976, pp. 365–382.

[29] K. Klöppel, J. Schubert, The calculation of the carrying capacity in the postbuckling range of thin-walled box columns loaded by concentric and excentric compressive force, Publications of the Institute for Statics and Steel Construction, Darmstadt.

[30] J. M. T. Thompson, G. M. Lewis, On the optimum design of thin-walled compression members, J. Mech. Phys. Solids 20 (2) (1972) 101–109.

[31] G. Kiymaz, FE based mode interaction analysis of thin-walled steel box columns under axial compression, Thin-Walled Struct. 43 (7) (2005) 1051–1070.

[32] H. Degée, A. Detzel, U. Kuhlmann, Interaction of global and local buckling in welded RHS compression members, J. Constr. Steel. Res. 64 (7) (2008) 755–765.

[33] B. Schafer, T. Peköz, Computational modeling of cold-formed steel: characterizing geometric imperfections and residual stresses, J. Constr. Steel. Res. 47 (3) (1998) 193–210.

[34] R. Cruise, L. Gardner, Measurement and prediction of geometric imperfections in structural stainless steel members, Struct. Eng. Mech. 24 (1) (2006) 63–89.

[35] A. Trouncer, K. Rasmussen, A rational procedure for modelling imperfections in advanced analysis of frames with locally unstable members, Thin-Walled Struct. 96 (2015) 183–201.

[36] J. Shen, M. A. Wadee, A. J. Sadowski, Interactive buckling in long thin-walled rectangular hollow section struts, Int. J. Non-Linear Mech. 89 (2017) 43–58.

[37] J. Shen, M. A. Wadee, Length effects on interactive buckling in thin-walled rectangular hollow section struts, Thin-Walled Struct. In press. 2017. doi:10.1016/j.tws.2017.04.006.

[38] E. J. Doedel, B. E. Oldeman, AUTO-07p: Continuation and bifurcation software for ordinary differential equations, available from http://indy.cs.concordia.ca/auto/ (2009).

[39] E. Riks, An incremental approach to the solution of snapping and buckling problems, Int. J. Solids Struct. 15 (7) (1979) 529–551.

[40] ABAQUS, Version 6.14, Dassault Systèmes, Providence RI, USA, 2014.

[41] B. W. Schafer, T. Peköz, Direct strength prediction of cold-formed steel members using numerical elastic buckling solutions, in: W. W. Yu, R. A. LaBoube (Eds.), Fourteenth International Specialty Conference on Cold-formed Steel Structures, Missouri S&T (formerly the University of Missouri-Rolla), 1998.

[42] P. S. Bulson, The stability of flat plates, Chatto and Windus, London, UK, 1970.

[43] G. W. Hunt, L. S. Da Silva, G. M. E. Manzocchi, Interactive buckling in sandwich structures, Proc. R. Soc. A 417 (1852) (1988) 155–177.

[44] M. A. Wadee, M. Farsi, Local–global mode interaction in stringer-stiffened plates, Thin-Walled Struct. 85 (2014) 419–430.

[45] L. Bai, M. A. Wadee, Mode interaction in thin-walled I-section struts with semi-rigid flange-web joints, Int. J. Non-Linear Mech. 69 (2015) 71–83.

[46] J. Shen, M. A. Wadee, A. J. Sadowski, Numerical study of interactive buckling in thin-walled section box columns under pure compression, in: D. Camotim, P. B. Dinis, S. L. Chan, C. M. Wang, R. Goncalves, N. Silvestre, C. Basaglia, A. Landesmann, R. Bebiano (Eds.), Proceedings of the 8th International Conference on Advances in Steel Structures (ICASS' 2015), 2015, paper number: 44.

[47] W. T. Koiter, On the stability of elastic equilibrium, Ph.D. thesis, Delft University of Technology, (An english translation is available as NASA, Tech. Trans., F 10, 833, 1967.) (1945).

[48] P. Bijlaard, G. Fisher, Column strength of H-sections and square tubes in postbuckling range of component plates, Tech. rep., National Advisory Committee for Aeronautics (1953).

[49] G. J. Hancock, Nonlinear analysis of thin sections in compression, J. Struct. Div (ASCE) 107 (ST3) (1981) 455–471.

[50] B. Young, K. Rasmussen, Bifurcation of singly symmetric columns, Thin-Walled Struct. 28 (2) (1997) 155–177.

[51] M. K. Wadee, G. W. Hunt, A. I. M. Whiting, Asymptotic and Rayleigh–Ritz routes to localized buckling solutions in an elastic instability problem, Proc. R. Soc. A 453 (1965) (1997) 2085–2107.

[52] H. Wu, J. Yang, S. Kitipornchai, Imperfection sensitivity of postbuckling behaviour of functionally graded carbon nanotube-reinforced composite beams, Thin-Walled Struct. 108 (2016) 225–233.

[53] J. M. T. Thompson, G. W. Hunt, Elastic instability phenomena, Wiley, London, 1984.

[54] S. P. Timoshenko, S. Woinowsky-Krieger, Theory of plates and shells, McGraw-Hill, New York, 1959.

[55] M. A. Wadee, L. Gardner, Cellular buckling from mode interaction in I-beams under uniform bending, Proc. R. Soc. A 468 (2137) (2012) 245–268.

[56] E. L. Liu, M. A. Wadee, Geometric factors affecting I-section struts experiencing local and strong-axis global buckling mode interaction, Thin-Walled Struct. 109 (2016) 319–331.

[57] G. W. Hunt, M. A. Peletier, A. R. Champneys, P. D. Woods, M. A. Wadee, C. J. Budd, G. J. Lord, Cellular buckling in long structures, Nonlinear Dyn. 21 (1) (2000) 3–29.

[58] P. Glendinning, Stability, instability and chaos: an introduction to the theory of nonlinear differential equations, Vol. 11 of Cambridge Texts in Applied Mathematics, Cambridge University Press, 1994.

[59] A. van der Neut, The sensitivity of thin-walled compression members to column axis imperfection, Int. J. Solids Struct. 9 (8) (1973) 999–1011.

[60] L. Bai, M. A. Wadee, Slenderness effects in thin-walled I-section struts susceptible to local–global mode interaction, Eng. Struct. 124 (2016) 128–141.

[61] MATLAB, version 7.10.0 (R2012a), The MathWorks Inc., Natick, Massachusetts, 2010.

[62] T. Belytschko, W. K. Liu, B. Moran, K. Elkhodary, Nonlinear finite elements for continua and structures, Wiley, New York, 2000.

[63] G. Garcea, L. Leonetti, D. Magisano, R. Gonalves, D. Camotim, Deformation modes for the post-critical analysis of thin-walled compressed members by a Koiter semi-analytic approach, Int. J. Solids Struct. 110-111 (2017) 367–384.

[64] E. Liu, Interactive buckling in thin-walled I-section struts of uniform thickness, Ph.D. thesis, Imperial College London (2016).

[65] W. J. Supple, Coupled branching configurations in the elastic buckling of symmetric structural systems, Int. J. Mech. Sci. 9 (2) (1967) 97–112.

[66] B. W. Schafer, Review: The Direct Strength Method of cold-formed steel member design, J. Constr. Steel. Res. 64 (78) (2008) 766–778.

[67] E. de Miranda Batista, Local–global buckling interaction procedures for the design of cold-formed columns: Effective width and direct method integrated approach, Thin-Walled Struct. 47 (11) (2009) 1218–1231.